Advances in Transporting and Processing Fuel Resources with Long-chain Hydrocarbons and Fatty Acids

by

Yingda Lu

A dissertation submitted in partial fulfillment
of the requirements for the degree of
Doctor of Philosophy
(Chemical Engineering)
in the University of Michigan
2015

Doctoral Committee:

       Professor H. Scott Fogler, Co-Chair
       Emeritus Professor Phillip E. Savage, Co-Chair
       Professor Arvind Atreya
       Professor Johannes W. Schwank

This dissertation is dedicated to my parents as well as my girlfriend Yu Du for their

unconditional love and support.

ACKNOWLEDGEMENTS

This dissertation would not have been possible without the support and contribution of many individuals throughout my doctoral study. I would first like to thank Professor H. Scott Fogler and Professor Phillip E. Savage, my research co-advisors and the co-chair of my doctoral committee, for their great commitment and help. I feel extremely fortunate to be co-advised by two brilliant minds. The vast knowledge they have in their respective fields has guided me through my study, and the kindest encouragement and support they gave has made me stronger on many levels. Professor Johannes W. Schwank and Professor Arvind Atreya, who both served in my doctoral committee, greatly helped my dissertation with their prominent attainments. I am grateful for their valuable insights.

I would also like to acknowledge my colleagues in Professor Fogler and Professor Savage's research groups. The early advices that Dr. Zhenyu Huang gave me were invaluable in building up my research skills; the numerous research discussions that I had with Sheng Zheng were always enjoyable and unforgettable; the generous assistance from Dr. Michael Hoepfner, Dr. Nasim Haji Akbari Balou, and Dr. Bobby Levine was always inspirational.

My sincere gratitude also goes to the excellent staffs of the Chemical Engineering Department: Laura Bracken, Michael Africa, Shelly Fellers, Kelly Raickovich, Susan Hamlin, and Laurel Neff, for they are patient, thoughtful, and friendly in every single day.

TABLE OF CONTENTS

LIST OF FIGURES

LIST OF TABLES

LIST OF APPENDICES

NOMENCLATURE

Geometry

d: diameter, m

r: radial coordinates (cylindrical coordinates), m

r_i: radius of the inner pipe, m

d_d: effective diameter of the pipe due to deposition, m

r_d: effective radius of the pipe due to deposition, m

z: axial coordinate (cylindrical coordinates), m

λ: de-dimensionalized axial coordinate.

η: de-dimensionalized radial coordinate.

L: length of the pipe, m

Transport and Thermal Dynamic Properties

C: concentration of wax in oil, wt%

C_p: specific heat, J/kg/K

D_{wo}: diffusivity of wax in oil, m^2/s

D_{eff}: effective diffusivity of wax in the deposit, m^2/s

$\overline{F}_w$: wax fraction of the deposit

Q_{oil}: volumetric oil flow rate, m^3/h

T: temperature, ℃ or K

U: averaged velocity, m/s

V: averaged velocity of oil, m/s

Gz_t: a form of the Graetz number in turbulent flow

J: mass flux, kg/m^2/s

V_A: molecular volume of wax, cm^3/mol

h: heat transfer coefficient, W/m^2/K

k: thermal conductivity, W/m/K

m: mass, g

t: time, s

y^+: dimensionless distance from the wall

μ : viscosity, Pa s

ρ : density, kg/m^3

δ : deposit thickness, mm

ε_{mass} : eddy diffusivity (momentum, heat or mass), m^2/s

τ : shear stress, Pa

Subscripts

oil: properties of the bulk oil

coolant: properties of the coolant

inlet: properties of the oil inlet of the pipe

interface: properties of the oil-deposit interface

wall: properties at the wall

dep: properties of the deposit

Abbreviations

HTC: hydrothermal carbonization.

LEH: lipid-extracted hydrochar.

SCW: supercritical water.

SCWG: supercritical water gasification.

EPA: eicosapentaenoic acid

ABSTRACT

Advances in Transporting and Processing Fuel Resources with Long-chain Hydrocarbons and Fatty Acids

By

Yingda Lu

Chair: H. Scott Fogler and Phillip E. Savage

This dissertation is devoted to two topics in fuel resources transporting and processing: one is to enhance the understanding of wax deposition in subsea oil transportation pipelines and the other is to make biofuels from microalgae while also producing nutraceuticals as high-value byproducts.

The first half of this dissertation highlights important aspects of wax deposition behaviors when operation conditions (i.e., temperature and flow rate) vary, which were previously overlooked or misinterpreted. We first found that the mass driving force and the shape of the solubility curve are the most important factors affecting deposition rates when operation temperature varies in addition to the "thermal driving force" used in most

previous studies. To capture the impact of the solubility curve on wax deposition, we established a new criterion to predict the rate of wax deposition when the operation temperatures change. This criterion could provide consistent prediction with the experimental observation and was proved to be a more sophisticated predictor compared to the previous one of thermal driving force.

Next, we provided an alternative explanation for the experimental trend of a reduced deposit with an increasing flow rate that has been frequently observed. Despite many previous studies intuitively attribute the reason to "shear removal", we identified three heat and mass transfer effects affecting and governing deposition behavior. These effects focus on the heat and mass transfer phenomena at the oil-deposit interface. In addition, the work revealed that the dynamics of the competition between these three effects can vary as time progresses and that the overall behavior of the wax deposit growth is eventually determined by the most dominant effect of the three.

Another piece of the dissertation focused on developing methods to promote the production of biofuels and nutraceuticals from microalgae. Microalgae has been gaining attention as a promising feedstock for renewable fuels and chemicals, but to date it is still difficult to commercialize this route due to the high cost and the technology challenges associated with producing algal oil. We first proved that hydrothermal carbonization (HTC) followed by warm ethanol extraction can recover ~75% of the fatty-acid-containing lipids from wet algae using only water and a non-petroleum-derived solvent. The recovered lipids include both those suitable for making liquid biofuels and those suitable for making dietary supplement (i.e., nutraceuticals). We then demonstrated for the first time that the lipid-extracted algal hydrochar (LEH), can be gasified in

supercritical water to recover energy (in the form of fuel gases) for use within a biorefinery and to recycle nitrogen (in the form of ammonium) for algae growth. Notably, ~75% energy recovery and ~100% nitrogen recovery as ammonium were achieved after gasification at 600 ℃ and 6 h.

CHAPTER 1

Introduction

1.1 Background

Fuels are materials with high energy density that can store and release energy to produce power or heat. From traditional resources such as wood and coal, to many alternatives like solar or nuclear, people have been exploring and using fuel resources since the dawn of humanity. Fuels play a critical role in the development of economy, culture and society. Over the last 200 years, world population has increased about 7 times; meanwhile the global energy consumption has inflated more than 20 times. With the continuous growth, by 2030, the world will need at least 45 percent more energy.[1] Producing and delivering this additional amount of energy has become one of the top concerns that clouds our way to prosperity.

One way to tackle this conundrum is to reduce the cost associated with energy production from raw fuel resources. As most types of raw fuel materials are undesirable for direct use, they have to be transported to different locations and processed into more preferable forms. Additional energy and efforts typically need to be spent on transporting fuel resources and addressing the problems that emerge during transportation. Taking petroleum as an example, the petroleum crudes produced from off-shore reservoirs

usually need to be transported in subsea oil transportation pipelines to on-shore refining facilities, where they will be further processed to final fuels such as gasoline or diesel. Due to the low temperature of sea water, a variety of flow assurance problems, such as wax deposition and asphaltene deposition, could occur during the transportation, resulting in a huge economical loss for industry.[2-3] For instance, the cost of remediating wax deposition during the transportation of petroleum crudes is on the order of $1,000,000, and this cost is proportionally greater as development depth increases.[4] Despite research efforts for decades, some of these problems still remain a challenge during fuel production and require further investigation.[5]

Another approach to satisfy the growing energy demand is to find alternative fuel resources. The conversion of biomass resources to fuels (e.g., biofuels) has been considered as a promising alternative to the production of fuels from petroleum.[6] Since the carbon released during the combustion of biofuels is biogenic, it does not increase the net concentration of greenhouse gases in the atmosphere over human time scales. To date, the two most widely used biofuels are ethanol, derived from fermenting sugarcane and corn, and biodiesel, produced by transesterifying vegetable oils from soybean, rapeseed, palm, and similar oilseeds. Despite substantial investment and policy support, their production to date has been relatively small and resource intensive, and cannot sustainably meet society's demand for fossil fuel alternatives.[7]

This dissertation is devoted to two topics in fuel resources transporting and processing: wax deposition in subsea oil transportation pipeline, and nutraecutical and biofuel production from algae feedstock.

1.2 Overview of Wax Deposition

Waxes, also known as n-paraffins, are a group of n-alkanes with carbon numbers usually greater than 20 and they are natural components of most crude oils and gas condensates.[8] As the on-shore reservoirs become depleted over time, the focus of oil production has shifted towards off-shore reservoirs. The petroleum fluids produced from off-shore reservoirs are usually transported to on-shore processing facilities through subsea oil transportation pipelines. Depending on the location of the platform, the subsea pipelines can range from tens to hundreds of kilometers. The oil typically leaves the reservoir at a temperature around 160 °F and is cooled significantly as it is transported through pipelines on the ocean floor where the water temperature is around 40 °F. As the oil temperature decreases below the wax appearance temperature (WAT), the waxy components can precipitate out of the oil due to a reduced solubility, resulting in slurries in the oil flow that require higher pressure-drop for transportation. More importantly, if the precipitation of waxy components occurs on the inner surface of the pipe wall, wax deposit could form inside the pipelines. The problem of wax deposition in the subsea pipeline has caused a series of problems for the flow assurance industry, including increased pressure-drop needed for oil transportation and potential blockage of the pipeline. The formed wax deposits, if not addressed properly, could continue to grow and eventually block the pipelines.

One of the most frequently used methods to remediate wax deposition in subsea operations is called "pigging", which uses an inspection gauge with brushes or blades on its surface to scrape off the wax deposits on the wall. Pigging is a costly operation, and normal oil production is usually interrupted during the operation, further adding to the cost of this approach. Therefore, it is critical to have a comprehensive understanding of

the physics and chemistry of wax precipitation and deposition in the pipeline in order to develop economically viable prevention and remediation strategies. The research in the first half of the dissertation is devoted to understanding wax deposition behavior under different operation conditions, particularly temperatures and flow rates.

1.3 Algae as a Promising Biofuel and Nutraecutical Feedstock

Microalgae, microscopic photosynthetic organisms found in both marine and fresh water environments, are gaining interest as an attractive renewable feedstock for nutraceuticals and biofuels production. One of the most important advantages of microalgae is their fast growth rate. Microalgae can double their biomass within one day.[9] Also, microalgae can be grown on marginal lands through the construction of raceway ponds, which leads to little competition with croplands. According to a recent estimation of the land-use requirements of biofuel feedstocks, only 1.1-1.7% of the total U.S. cropland would be needed to meet 50% of the U.S. demand for transportation fuels when producing biodiesel from microalgae.[10] Furthermore, microalgae can be cultivated to contain diverse lipid contents and compositions through selective genetic and metabolic engineering.[11] These advantages give microalgae tremendous potential as a sustainable feedstock for a variety of lipid-derived products including fuels, pigments, pharmaceuticals, and cosmetics.

Although promising in principle, microalgae present unique challenges in practice. One major technical challenge in the process of producing algal oil is to extract efficiently and economically the lipids of interest from algal cells. Algal biomass naturally contains water and therefore usually needs to be dried prior to an extraction step. This drying step consumes a significant amount of energy that cannot easily be recovered because of the

low temperature at which it would be available. Such energy inputs need to be avoided or minimized. There is a clear need for a process that can obviate biomass drying but still offer high lipid recoveries from microalgae. These topics will be discussed in the second half of the dissertation.

1.4 Research Objectives

As outlined in preceding sections, this dissertation emphasizes two topics in fuel resources transporting and processing: wax deposition in subsea oil transportation pipeline, and nutraecutical and biofuel production from algae feedstock. The goal of the first work was to improve the current understanding of the deposition physics, therefore promoting advanced industrial design of appropriate remediation and prevention techniques. Chapter 2 and Chapter 3 report the findings for this work. The objective of the second work was to develop methods that could promote the production of biofuels and nutraceuticals from microalgae in a more sustainable and environmentally friendly manner. The results are presented in Chapter 4 and Chapter 5. The dissertation concludes with a summary of the findings, their significance to the field, and an outlook for the further research efforts.

CHAPTER 2

The Effect of Operating Temperatures on Wax Deposition

2.1 Introduction

2.1.1. Background

Wax deposition in the subsea pipelines is a major flow assurance problem in the petroleum industry. When crude oil at a high temperature (70-120 °C) from subsea reservoirs flows through the pipelines on the ocean floor (4 °C), the heat loss from the crude oil to the sea water causes wax molecules to deposit on the pipe wall.[12] The deposition poses a significant problem for petroleum transportation by creating flow constrictions that can increase the pressure drop in the pipe and increase the production cost. The deposit can even grow to a point where the pipeline becomes plugged, causing production to be stopped in order to replace the plugged portion of the pipeline.[13] The development and application of the remediation techniques for wax deposition have become a vital part of the flow assurance practice and research. Significant production cost can be attributed to these techniques include pigging, pipeline insulation, heating and fused chemical reactions.[14] Using pigging as an example, insufficient pigging frequency can result in a deposit that grows so thick that the pig has been known to get stuck, which

6

stops the flow of petroleum fluids. However, too high of a pigging frequency can lead to additional costs of tens of millions of dollars due to deferred production.[15] To arrive at an optimal pigging frequency, the rate of wax deposition needs to be determined. This rate of deposition is thought to change along the axial direction in a subsea pipeline because of continuous heat loss of the crude oil.[16] The loss of heat in the oil causes the variation in the temperature gradient along the pipe, which alters the driving force for wax deposition.[17]

To study the wax deposition in the subsea pipelines, many lab-scale experimental studies have been carried out for different operating temperatures.[4,18-20] Cold-finger and flow-loop experiments are the two commonly used apparatus. In cold-finger experiments, a small cylindrical metal heat exchanger (the cold-finger) is maintained at a lower temperature and is submerged in a bulk crude oil of a higher temperature. The temperatures of the cold-finger and the bulk crude oil are controlled by two separate water baths. By changing the bulk oil temperature and the cold-finger temperature, the wax deposition can be studied for different thermal gradients.[18,19] Although the cold-finger experiments provide some insights on wax deposition, they certainly are not a direct representation of wax deposition in field-scale pipelines because of the difference in geometries and flow fields between a cold-finger system and pipe-flow system.[4] The flow-loop apparatus better simulates the conditions for wax deposition in subsea pipelines compared to cold-finger devices. Most flow-loops are equipped with an annular pipe where the crude oil flows in the inner pipe while the coolant flows through the annulus. By changing the temperatures of the oil and the coolant, the thermal conditions at different axial positions of the subsea pipeline can be simulated.[4,17,20] In these studies

described above, the temperature difference between the bulk oil and the coolant (or the cold finger temperature) is frequently referred to as the "thermal driving force" for wax deposition. A comparison of these studies is discussed to review the wax deposition characteristics for different temperature conditions.

2.1.2. Decreasing Wax Deposition with Decreasing Thermal Driving Force

Jennings et al. used a cold-finger apparatus and a crude oil from the Gulf of Mexico to study wax deposition at different cold-finger temperatures while the bulk temperature of oil was kept constant.[18] It was found that the experiments with higher cold-finger temperatures (smaller thermal driving force) yielded smaller amounts of deposit. Creek et al. found similar results using a flow-loop apparatus to study wax deposition for different coolant temperatures.[4] Their study showed a decrease of the deposit thickness when the coolant temperature increased (decreasing thermal driving force). In the study of Bidmus et al., four different inlet temperatures were examined while the coolant temperature was kept constant. It was found that a decrease in the oil temperature (decreasing thermal driving force) to near ambient or pipe-wall temperatures could substantially decrease wax deposition. In all the above studies, a generalization was made that the deposit thickness decreases when thermal driving force decreases. In the above studies, the focus on the thermal driving force for wax deposition is based on the fact that molecular diffusion was regarded as the most prevalent mechanism for a variety of wax deposition studies. [4,8,17-22] In this mechanism, the mass flux of the wax molecules at the interface (from the oil towards the deposit) $D_{wo,\,interface} \left. \dfrac{dC}{dr} \right|_{from\ oil\ to\ interface}$ represents the loss of wax from the oil to form a deposit. Among the parameters in the mass flux, the concentration gradient

$\left.\dfrac{dC}{dr}\right|_{\text{from oil to interface}}$ can be approximated by applying the chain rule and using two

parameters: the radial temperature gradient, $\left.\dfrac{\partial T}{\partial r}\right|_{\text{from oil to interface}}$, and the solubility gradient,

$\left.\dfrac{dC}{dT}\right|_{\text{from oil to interface}}$, as shown in Equation (1).

$$D_{\text{wo, interface}}\left.\frac{dC}{dr}\right|_{\text{from oil to interface}} \approx D_{\text{wo, interface}} \cdot \left(\left.\frac{dT}{dr}\right|_{\text{from oil to interface}}\right) \cdot \left(\left.\frac{dC}{dT}\right|_{\text{from oil to interface}}\right) \quad (1)$$

The first term of the RHS of Equation (1), namely the radial temperature gradient, has been the focus in previous studies where the thermal driving force has been consider as the major parameter to explain the temperature effects on wax deposition.[4,18,20] However, equally important is the solubility gradient at the oil-deposit interface, that is, the second parameter on the RHS of Equation (1), and it is frequently overlooked in theoretical analyses. The solubility gradient reflects the effect of the effect of the solubility curve on wax deposition. For particular types of oil, the impact on the solubility curve can overcome the effect of the temperature gradient when the operating conditions change.

2.1.3. Increasing Wax Deposition with Decreasing Thermal Driving Force

Cold-finger studies by Paso and Fogler on other oils at lower temperatures showed an opposite trend to that discussed above, where more wax molecules can precipitate and form thicker deposits with decreasing temperature gradients.[19] This trend was attributed to a result of an increase in the wax precipitation at the cold-finger surface, which was not accounted for in any of the previous studies. However, this trend had not been previously observed in flow-loop experiments, until this work.

2.2 Wax Deposition Experiments

In the study reported here, experiments consist of a series of experiments carried out using a laboratory flow-loop in the Herøya Research Center of Statoil ASA in Porsgrunn, Norway. An oil from the North Sea identified as North Sea Oil A is provided by Statoil ASA and is used in this study for deposition experiments. In addition, the experimental results in a previous study by Bidmus et al.[20] using a model oil-wax system will be used as a comparison in this study. Because the solubility curve of the model oil used in the study of Bidmus et al was not provided, it was measured in the current study using differential scanning calorimetry (DSC).

2.2.1. Flow-loop Experiments with North Sea Oil A
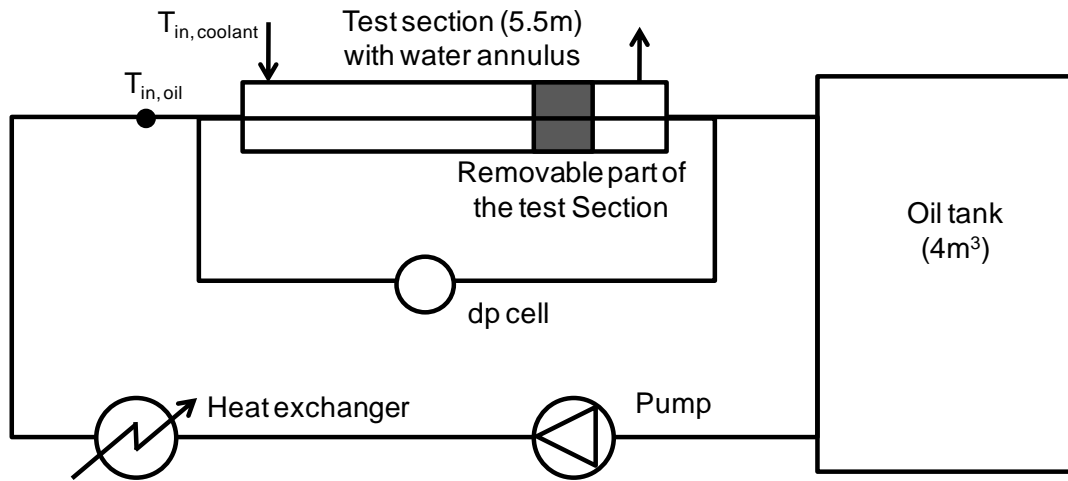
Figure 1: Schematic of the flow-loop experiment for wax deposition[21]

A sketch of the flow-loop from the Herøya Research Centre of Statoil ASA is shown in Figure 1. The flow-loop is equipped with a reservoir of 4 m^3 and a test section with a length of 5.5 m and an inner diameter (i.d.) of 5.3 cm. The deposit thickness was calculated from pressure-drop measurements in the test section. The values of the calculated wax thickness were confirmed by laser measurements of the wax in the oil-deposit at the end of an experiment. The detail information of flow-loop along with the

10

characterization techniques to study wax deposition have been reported by Hoffmann and Amundsen.[21]

The North Sea Oil A used for this research has a cloud point of approximately 30 °C. The amount of precipitation of wax in the oil at various temperatures was measured using the centrifugation and gas chromatography techniques, as reported by Han and Fogler and shown in Figure 2.[22]
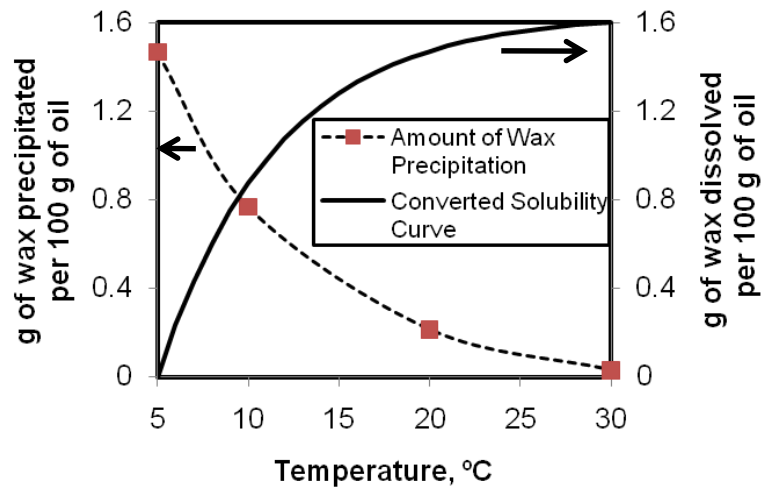
Figure 2: The amount of precipitation of wax in oil at various temperatures and the corresponding solubility curve for the North Sea Oil A.

The solubility curve of the North Sea Oil A is an important input parameter for wax deposition modeling. It was obtained by assuming that all the wax in the end has precipitated out of the oil at 5 °C. In this case the total wax content is the same as the precipitation of wax at 5 °C, as shown in Figure 2. Because the coolant temperatures of all the experiments are no less than 5 °C, the wall temperatures of all the experiments are higher than 5 °C. Because the temperature of the wall is the lowest point in the flow-loop system, the amount of wax precipitation in this North Sea oil A below the wall temperature is not needed for model predictions in this study. Similarly, the solubility

curve for the model oil is shown for the temperature above 25 °C in Figure 4, which is the coolant temperature in the corresponding experiments.
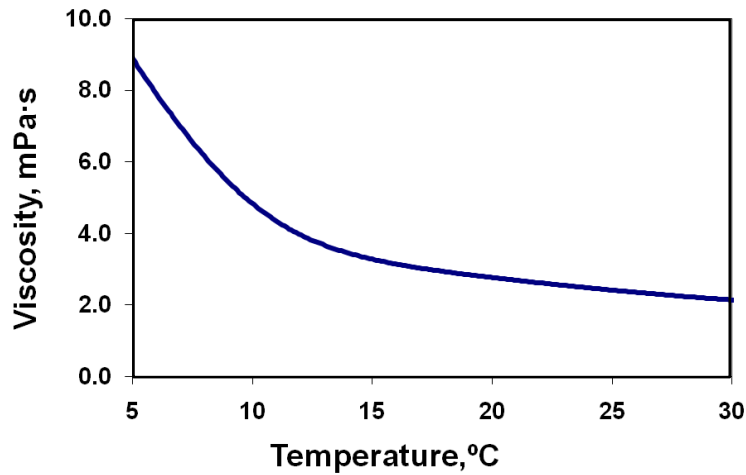
Figure 3: The viscosity of North Sea Oil A at different temperatures

In addition, the viscosity of the North Sea Oil A was measured as a function of temperature using a Physia MCR 301 Rheometer. The viscosity-temperature curve is shown in Figure 3.

2.2.2. The Solubility Curve of the Model Oil in the study of Bidmus et al.[20]

A previous study by Bidmus et al. using a model oil with 6% wax content and a cloud point of 35 °C was chosen as the basis of comparison in this research. Most of the properties of this model oil can be found in the work of Bidmus et al.[20] However, the solubility of wax was not reported in their study. To measure this parameter, we purchased the same solvent, Norpar13 from Imperial Oil (Ontario, Canada), and the same wax sample, Parowax, from Conros Corp (Ontario, Canada), that were used by Bidmus et al. The solubility was measured with a TA Q2000 DSC. The oil was first heated to 60 ˚C and held at this temperature for half an hour to remove any thermal history and then cooled from 60˚C to -40˚C at a rate of 1˚C/min. The solubility curve of the model oil was

12

obtained assuming that the heat release is proportional to the amount of precipitated wax, as shown in Figure 4.
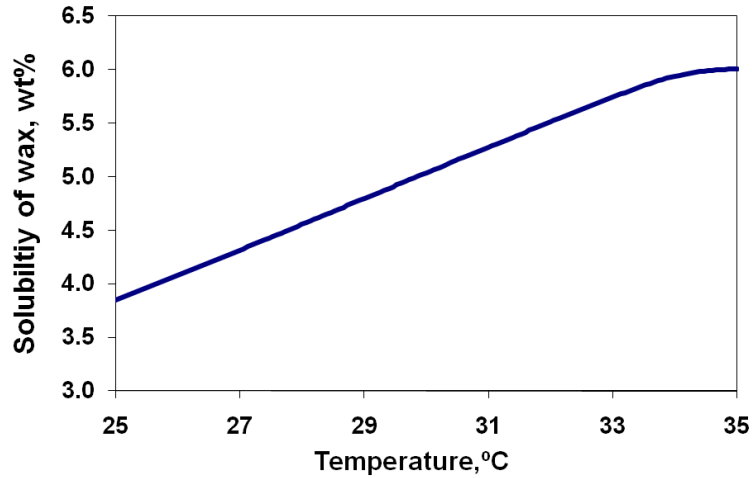
Figure 4: The solubility curve of wax for the model oil

Comparing Figure 2 and Figure 4, it can be noted that as the oil is cooled, the solubility of the model oil is not as temperature-sensitive as the North Sea Oil A.

2.3 Theoretical Analysis using The Michigan Wax Predictor (MWP)

2.3.1. Model introduction

The mathematical model called the Michigan Wax Predictor (MWP) based on earlier studies of Singh, Lee, Huang and Fogler was applied to investigate the temperature effects on wax deposition.[8,12,17] The MWP applies the Graetz boundary conditions and the flow of the oil is assumed to be in a quasi-steady state while the wax thickness, δ, increases with time. The external heat transfer coefficient for the coolant was calculated using the correlation by Monrad and Pelton to account for the heat loss to the coolant flowing in the annuli of the pipe.[23] The internal heat and mass transfer rates were calculated using a 2D axial symmetry energy equation and the correlation for eddy diffusivity by Van Driest.[24] The model calculates the axial convection and the radial conduction/diffusion for the heat and mass transfer equations to determine the

13

temperature profile as well as the concentration profile of wax molecules, as shown in Figure 5.
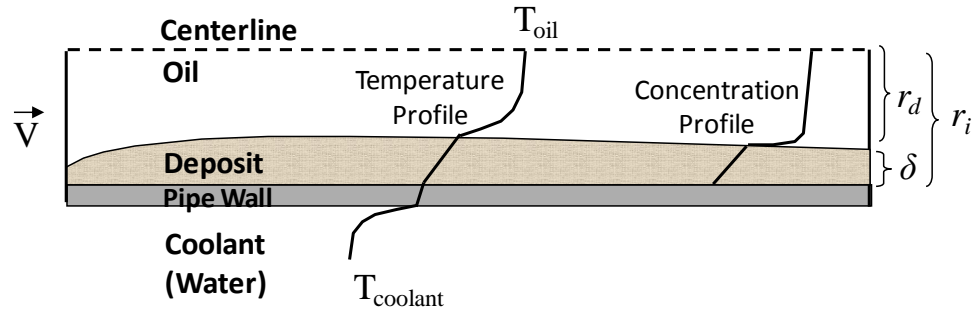
Figure 5: Sketch of wax deposition mechanism.

With the information of the concentration profile, the concentration gradient at the interface is thereby determined to calculate the growth rate of both the deposit thickness and the wax fraction in the deposit, using molecular diffusion as the major mechanism for wax deposition. The details of this model can be found in the work of Lee and Huang et al.[8,12]

It should be noted that the equations in the model were developed from first principles and that no tuning parameters were used. In this analysis of mass transfer, it is assumed that wax molecules only precipitate in the deposit and that they do not precipitate in the oil phase. This approach is similar to the one used in the laminar flow model by Singh and Fogler where the heat and mass transfer correlations were decoupled.[17] In addition, the model in the current study does not need to incorporate the so-called "shear removal" effect, i.e. the detachment of the deposited wax material from the pipe wall by the flowing oil in order to predict the observed trends. Because the effect of bulk precipitation and shear removal are highly empirical, the use of tuning parameters to include these effects can reduce the reliability for our conclusions. Consequently, the major focus of this model is to examine a number deposition experiments in general to

14

learn if the model represents the trends shown in the experiments rather than comparing each experiment with their corresponding model predictions.

2.3.2. Determining parameter for wax deposition

To look for a more representative driving force for wax deposition than the thermal driving force, the MWP analyzes the mass balance equation shown in Equation (2) along with the boundary conditions shown in Equation (3)

$$V \frac{\partial C}{\partial z} = \frac{1}{r} \frac{\partial}{\partial r} \left[(\varepsilon_{mass} + D_{wo}) r \frac{\partial C}{\partial r} \right] \tag{2}$$

$$\begin{cases} \text{at } z = 0,\ C = C_{inlet} \\ \text{at r = 0, } \frac{\partial C}{\partial r} = 0 \\ \text{at r = } r_d,\ C = C_{interface} \end{cases} \tag{3}$$

The following dimensionless ratios given in Equation (4) were used to de-dimensionalize the mass balance equation and the boundary conditions shown in Equations (2) and (3), resulting in Equations (5) and (6).

$$\left(\theta = \frac{C - C_{interface}}{C_{inlet} - C_{interface}} \right), \left(v = \frac{V}{U} \right), \left(\lambda = \frac{z}{L} \right), \left(\eta = \frac{r}{r_d} \right), \left(Gz_t = \frac{d_d^2 U}{L(\varepsilon_{mass} + D_{wo})} \right) \tag{4}$$

$$v \frac{\partial \theta}{\partial \lambda} = \frac{1}{\eta} \frac{\partial}{\partial \eta} \left[\frac{4}{Gz_t} \eta \frac{\partial \theta}{\partial \eta} \right] \tag{5}$$

$$\begin{cases} \text{at } \lambda = 0,\ \theta = 1 \\ \text{at } \eta = 0,\ \frac{\partial \theta}{\partial \eta} = 0 \\ \text{at } \eta = 1,\ \theta = 0 \end{cases} \tag{6}$$

One notes that the solution profile of the de-dimensionalized variable θ from Equations (5) and (6), is independent of the changes in C_{inlet} and $C_{interface}$. Consequently, the radial mass flux of wax molecules from the bulk towards the interface can be found to be proportional to $[D_{wo, interface} (C_{inlet} - C_{interface})]$, as given by Equation (7).

15

$$D_{wo,\,interface} \left. \frac{dC}{dr} \right|_{interface} = D_{wo,\,interface} \frac{\partial C}{\partial \theta} \cdot \left(\left. \frac{\partial \theta}{\partial r} \right|_{interface} \right) =$$

$$\frac{D_{wo,\,interface} \left(C_{inlet} - C_{interface} \right)}{r_d} \left(\left. \frac{\partial \theta}{\partial \eta} \right|_{interface} \right) \tag{7}$$

The impact of temperature on the concentration differences, (C_{inlet} - $C_{interface}$) can be seen by assuming thermodynamic equilibrium for the concentrations, in which case the solubility curve of the oil can be used to obtain a form of a mass flux, J, as given in Equation (8).

$$J = \frac{D_{wo,\,interface} \left(C_{inlet} - C_{interface} \right)}{r_d} \approx \frac{D_{wo,\,interface} \left[C_{inlet} \left(eq \right) - C_{interface} \left(eq \right) \right]}{r_d} \tag{8}$$

In addition, the effect of the temperature on the diffusivity can be estimated using the Hayduk-Minhas correlation as shown in Equation (9).[25]

$$D_{wo,interface} = 13.3 \times 10^{-12} \frac{T_{interface}^{1.47} \mu^{(10.2/V_A - 0.791)}}{V_A^{0.71}} \; m^2/s \tag{9}$$

Difficulties arise when one tries to evaluate $D_{wo,\,interface}$ and $C_{interface}(eq)$ because they depend on the interface temperature, $T_{interface}$ which in turn greatly depends on the predicted value of an existing deposit thickness. Therefore one needs to know the exact thickness of the deposit in order to accurately determine $C_{interface}(eq)$ and $D_{wo,\,interface}$. This hurdle can be resolved by evaluating the values of $D_{wo,\,interface}$ and $C_{interface}(eq)$ initially (at t=0 and δ=0), where deposition has not yet occurred. In this case $C_{interface}(eq)$ simply reduces to $C_{wall}(eq)$, $D_{wo,\,interface}$ reduces to $D_{wo,\,wall}$ and r_d reduces to r_i. Because the wall temperature, T_{wall}, can be accurately determined by solving the heat transfer equation in the MWP using well established correlations for the eddy diffusivities,[24] $C_{wall}(eq)$ can be obtained from T_{wall}, knowing the solubility curve of the oil, and $D_{wo,\,wall}$ can be determined through T_{wall} using the Hayduk-Minhas correlation.[25] It should be noted that

in most of the lab-scale flow-loop studies, no significant axial variations in the bulk concentration were observed for the parameters as a result of the short length of the pipe. Therefore, $C_{inlet}(eq)$ is referred to as $C_{oil}(eq)$, for subsequent quantitative analyses.

The significance of the above analysis is that the impact of the oil/coolant temperatures on wax deposition can be found by investigating their effect on a parameter that has the unit of a mass flux, as shown in Equation (10)

$$J_{wax,c} = \frac{D_{wo,\,wall}\left[C_{oil}\left(eq\right) - C_{wall}\left(eq\right)\right]}{r_i} \tag{10}$$

Consequently, $J_{wax,c}$ is referred to as the characteristic mass flux for wax deposition. The difference in the concentrations, $[C_{oil}(eq) - C_{wall}(eq)]$, is referred to as the mass driving force in comparison of the thermal driving force ($T_{oil} - T_{coolant}$) among several deposition studies.[4,18,20] We will show that this mass driving force is the most dominant parameter to affect the behavior of the mass flux for wax deposition, $J_{wax,c}$, when the oil/coolant temperatures are changed. It was found that the conclusions for $J_{wax,c}$ at t=0 (δ=0) also hold for t>0 (δ>0). The details of this verification can be found in Appendix A.

2.4 Results and Discussions

2.4.1. Flow-loop Results and Prediction of the Experimental Trends by Model

Several experimental studies have found that the amount of deposit decreases with decreasing thermal driving force.[4,18,20] However, Figures 6 and 7 show the experimental and theoretical trajectories of wax thickness as a function of time for different operating temperature conditions. The experiments carried out in the current study have shown the two following opposing trends:
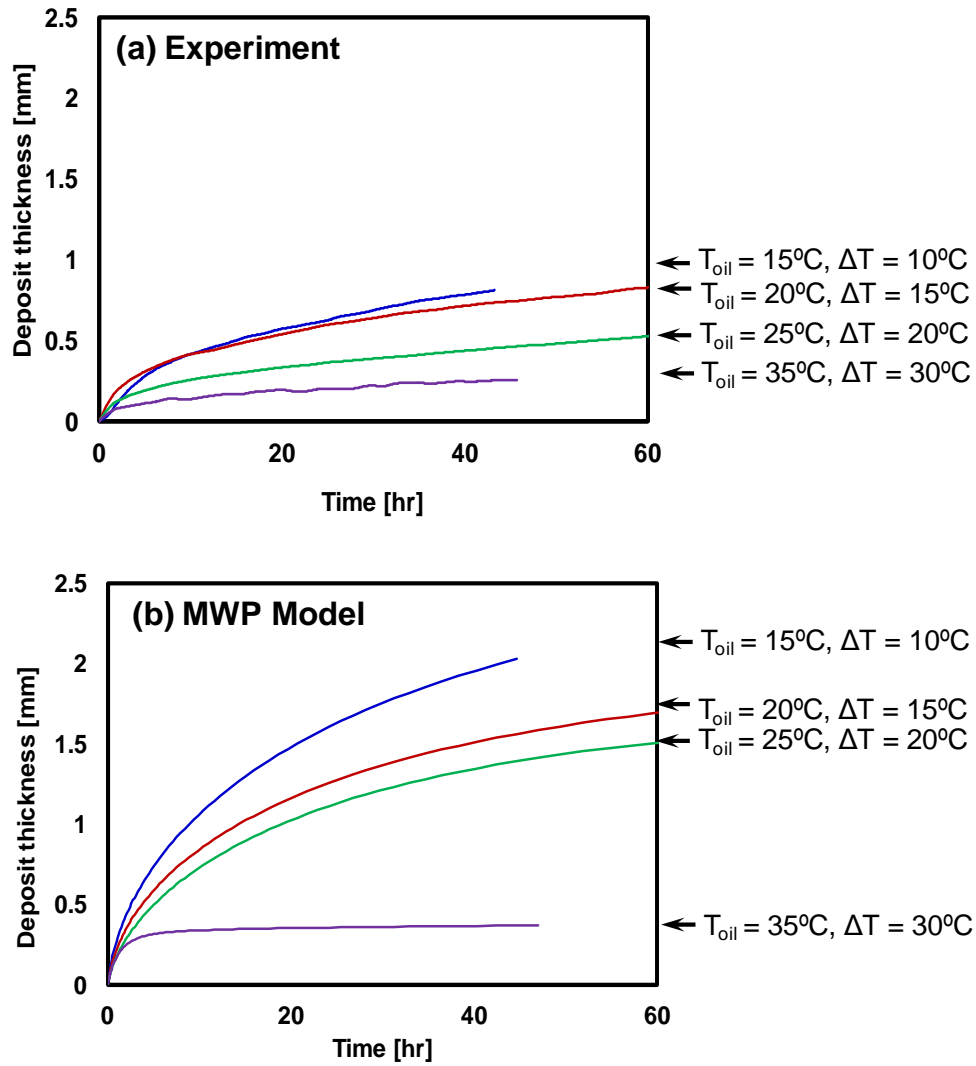
Figure 6: Comparison of deposit thickness as a function of oil temperature, T_{oil} between (a) the experimental results and (b) the model prediction by the MWP. The oil flow rate, Q_{oil}, was maintained constant at $20m^3/h$ and the coolant temperature, $T_{coolant}$, was maintained constant at 5 °C.
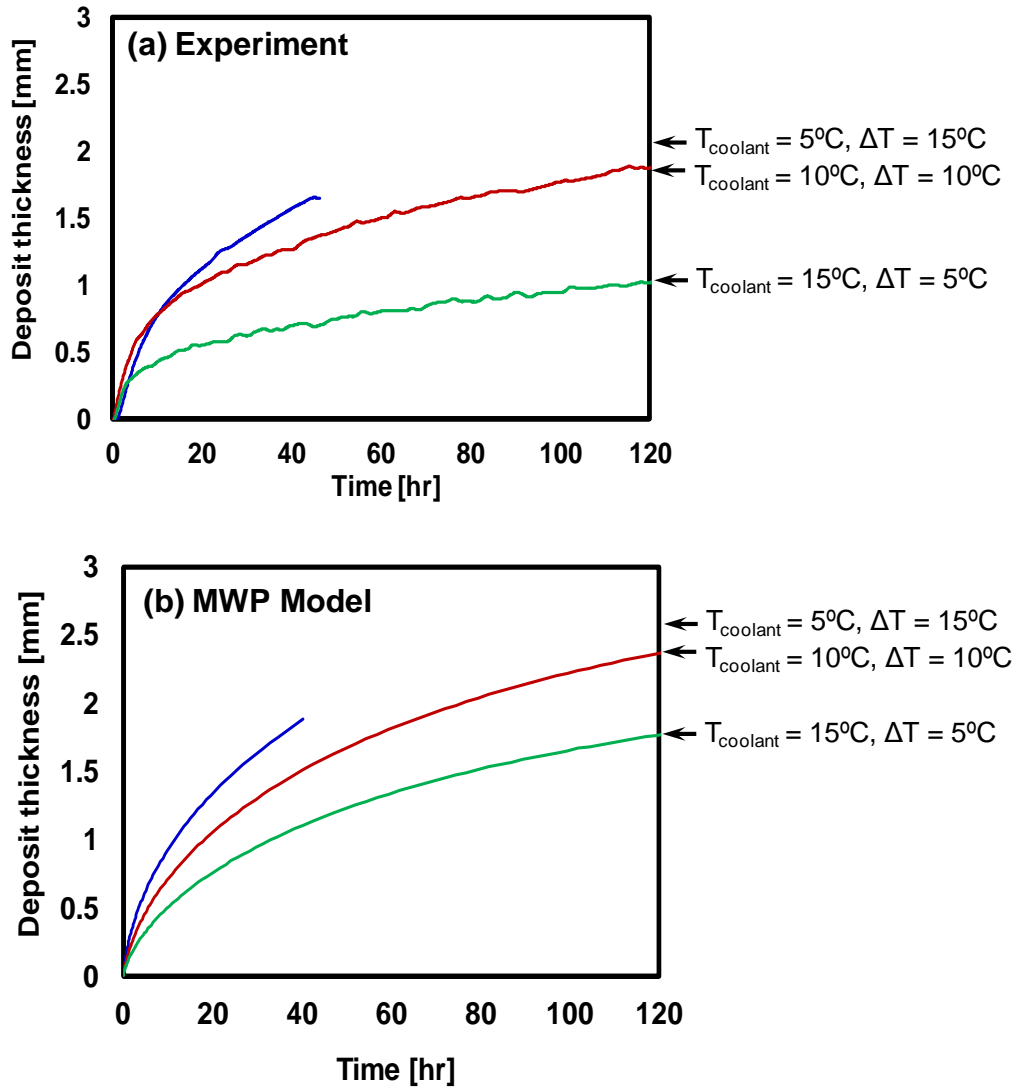
Figure 7: Comparison of deposit thickness as a function of coolant temperature, $T_{coolant}$, between (a) the experimental results and (b) the model prediction by the MWP. The oil flow rate, Q_{oil}, was maintained constant at 5m³/h and the oil temperature, T_{oil}, was maintained constant at 20 ℃.

Trend (1) (Figure 6): Reduced deposition with increasing oil temperature, T_{oil}, that is,

increasing thermal driving force (T_{oil} - $T_{coolant}$).

Trend (2) (Figure 7): Reduced deposition with increasing coolant temperature, $T_{coolant}$,

that is, decreasing thermal driving force (T_{oil} - $T_{coolant}$).

These two opposing trends indicate that the thermal driving force is not the best

candidate for a theoretical analysis of wax deposition, and other factors exists to better

explain the change of wax deposition at different oil temperatures. Because of the agreement of the trends between the experiments and the predictions by MWP Figures 6 and Figure 7, the MWP will be used to analysis the results shown in this study. In particular, the variations of the parameters in the characteristic mass flux for wax deposition, $J_{wax,c}$, for the experiments with different oil/coolant temperatures will be investigated. The parameters consist of the diffusivity, $D_{wo, wall}$ and the mass driving force, $[C_{oil}(eq) - C_{wall}(eq)]$.

2.4.1.1. Analysis for the Reduced Deposition with Increasing Oil Temperature

Table 1 summarizes the characteristic mass flux for wax deposition, $J_{wax,c}$ and its corresponding parameters for the experiments where the oil temperature, T_{oil} was varied and the coolant temperature, $T_{coolant}$ was kept constant. In these experiments, the deposition thickness decreased as the oil temperature increases as shown in Figure 6.

Table 1: Comparison of $J_{wax,c}$ among the deposition experiments with different $T_{oil,}$ while Q_{oil} and $T_{coolant}$ are maintained constant.

Parameters	Value			
Experimental Operating Conditions				
T_{oil}, ^{0}C	15.3	20.3	25.3	35.4
$T_{coolant}$, ^{0}C	5.0			
Q_{oil}, m^3/h	20.0			
Model Calulations				
T_{wall}, ^{0}C	9.5	12.0	14.7	20.5
$D_{wo,wall}$ ×10^{10}, m^2/s	2.11	2.49	2.89	3.64
C_{oil}(eq), wt%	1.09	1.26	1.34	1.44
C_{wall}(eq), wt%	0.65	0.89	1.07	1.26
C_{oil}(eq) - C_{wall}(eq), wt%	0.45	0.36	0.27	0.17
$J_{wax,c}$ ×10^{10}, m/s ·wt%	36.17	34.14	29.73	23.57

One observes that the increase in T_{oil} leads to an increase in T_{wall}, which in turn has several effects on the flux term, $J_{wax,c} = \{D_{wo, wall} \cdot [C_{oil} (eq) - C_{wall} (eq)]/r_i\}$: First, the

diffusivity of wax in oil at the wall, $D_{wo, wall}$ increases, which tends to increase the mass flux. Second, the changes in T_{oil} and T_{wall} causes the increases in both $C_{oil}(eq)$ and $C_{wall}(eq)$. Although the change in T_{oil} from 15.3 °C up to 35.4 °C (a change of 20.1 °C) exceeded the change in T_{wall} from 9.5 °C up to 20.5 °C (a change of 11 °C), the change in $C_{oil}(eq)$ from 1.09% to 1.44% (a change of 35%) was less than the change in $C_{wall}(eq)$ from 0.65% up to 1.26% (a change of 190%). Therefore, the mass driving force, $[C_{oil}(eq) - C_{wall}(eq)]$ decreases as the T_{oil} increases and outweighs the increase in $D_{wo, wall}$, resulting in a decrease in the characteristic mass flux, $J_{wax,c}$, as can be seen in the last row of Table 1. This decrease in the characteristic mass flux for wax deposition explains the reduced deposit thickness shown in Figure 6 for the experiments with increasing oil temperatures. It should be noted that the difference in the amount of change in the equilibrium concentrations at different temperatures (T_{oil} and T_{wall}) reflects the effect of the concave shape of the solubility curve (Figure 2) where its gradient decreases as temperature increases.

2.4.1.2. Analysis for the Reduced Deposition with Increasing Coolant Temperature

Now consider the other parameter variation where $T_{coolant}$ was varied and T_{oil} was kept constant. For these operating conditions it was found that the experimental wax thickness decreased as $T_{coolant}$ increased (Figure 7). The characteristic mass flux for wax deposition, $J_{wax,c} = \{D_{wo, wall} \cdot [C_{oil}(eq) - C_{wall}(eq)]/r_i\}$ and its corresponding parameters are shown in Table 2.

Table 2: Comparison of $J_{wax,c}$ among deposition experiments with different coolant temperatures, while Q_{oil} and $T_{coolant}$ are maintained constant.

Parameters	Value		
Experimental Operating Conditions			
T_{oil}, ^{0}C	20.2		
$T_{coolant}$, ^{0}C	5.0	10.0	15.0
Q_{oil}, m^3/h	5.0		
Model Calculations			
T_{wall}, ^{0}C	8.1	12.1	16.1
$D_{wo, wall} \times 10^{10}$, m^2/s	1.93	2.44	2.97
C_{oil} (eq), wt%	1.26	1.26	1.26
C_{wall} (eq), wt%	0.48	0.89	1.13
C_{oil} (eq) - C_{wall} (eq), wt%	0.78	0.37	0.13
$J_{wax,c} \times 10^{10}$, m/s ᐧwt%	57.35	34.39	14.71

It can be seen from Table 2 that the increase in $T_{coolant}$ leads to the increase in T_{wall}, which increased the values of both D_{wo} and C_{wall} (eq). The increase in D_{wo} tends to increase the characteristic mass flux, $J_{wax,c}$. However, the increase in C_{wall} (eq) from 0.48% to 1.13% causes significant decrease in the mass driving force [C_{oil} (eq) - C_{wall} (eq)] from 0.78% to 0.13%. This decrease in the mass driving force overcomes the increase in the diffusivity, leading to a decrease in the characteristic mass flux, $J_{wax,c}$, with increasing $T_{coolant}$, as is shown in the last row of Table 2. This decrease in $J_{wax,c}$ explains the reduced experimental deposit thickness, as shown in Figure 7.

2.4.1.3. Analysis of previous studies

The increase or decrease in the amount of wax deposit with the change in the temperature conditions can be attributed to the shape of the solubility curve, which causes the equilibrium concentration to behave differently in the bulk oil than at the wall. To further verify this result, the previous study on wax deposition by Bidmus et al[20] was analyzed. Figure 8 shows the experimental trends from the study of Bidmus et al. from a

flow loop with a test section of 2.54 cm i.d. and 10.16 cm length.[20] It can be seen that as T_{oil} increases the amount of deposit increases, which initially appears to be contradictory to the trend in our study as shown in Figure 6. However, when we applies the analysis on the characteristic mass flux for wax deposition, $J_{wax,c}$, the results are entirely consistent.
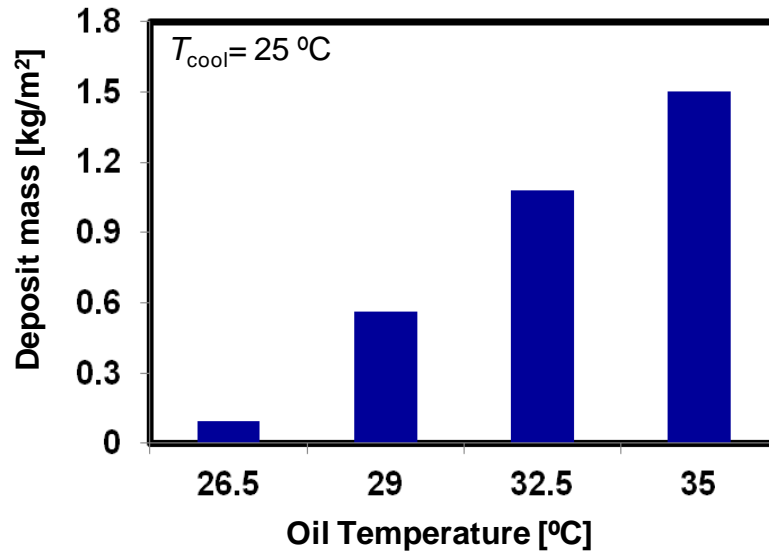
Figure 8: Comparison of the amount of deposit between experiments with different oil temperatures for the study of Bidmus et al.[20]

The parameters for the mass flux were calculated and shown in Table 3 on the basis of the geometry of the flow-loop and the operating conditions reported in their study.

Table 3: Comparison of $J_{wax,c}$ among deposition experiments with different T_{oil} while Q_{oil} and $T_{coolant}$ are maintained constant in the study of Bidmus et al using a model oil.

Parameters	Value			
Experimental Operating Conditions				
T_{oil}, ^{0}C	26.5	29.0	33.0	35.0
$T_{coolant}$, ^{0}C	25.0			
Q_{oil}, m^3/h	0.4			
Model Calculations				
T_{wall}, ^{0}C	25.4	25.9	27.1	28.0
$D_{wo, wall} \times 10^{10}$, m^2/s	2.81	2.94	3.27	3.53
C_{oil} (eq), wt%	4.19	4.80	5.74	6.00
C_{wall} (eq), wt%	3.94	4.05	4.34	4.55
C_{oil} (eq) - C_{wall} (eq), wt%	0.25	0.75	1.40	1.45
$J_{wax,c} \times 10^{10}$, m/s ·wt%	27.66	86.81	180.24	201.52

It can be seen that the increases of T_{oil} from 26.5 ℃ to 35 ℃ had two effects on increasing the mass flux. First, a increase in D_{wo} was observed, which tends to increase $J_{wax,c}$. Second, both C_{oil} (eq) and C_{wall} (eq) increased as a result of increased T_{oil} and T_{wall}. More importantly, the increase in C_{oil} from 4.19% to to 6.00% is greater than the increase in C_{wall} from 3.94% to 4.55%, which results in the increase in the mass driving force, [C_{oil} (eq) - C_{wall} (eq)]. The combination of the increases in the diffusivity and in the mass driving force results in the increase in the mass flux with increasing T_{oil}, which explains the experimental trends observed Figure 8 where the amount of deposition increases with increasing T_{oil}.

The importance in the solubility curve to affect the driving force for wax deposition can be seen by comparing experiments in this study (Figure 6 and Table 1) and those in the study of Bidmus et al. (Figure 8 and Table 3).[20] The changes in T_{oil}, T_{wall}, C_{oil} (eq) and C_{wall} (eq) for the two studies when T_{oil} was varied are shown in Table 4.

Table 4: Comparison of the changes in T_{oil}, T_{wall}, $C_{oil}(eq)$ and $C_{wall}(eq)$ for the experiments with both the North Sea Oil A and the Model oil where T_{oil} was varied. The numbers are calculated from Table 1 and Table 3.

	North Sea Oil A	Model Oil
Change in T_{oil}, ℃	15.3 ~ 35.4	26.5 ~ 35.0
ΔT_{oil}, ℃	20.1	8.5
ΔT_{wall}, ℃	11.0	2.6
$\Delta T_{oil} > \Delta T_{wall}$	Yes	Yes
ΔC_{oil} (eq), wt%	0.35	1.81
ΔC_{wall} (eq), wt%	0.61	0.61
ΔC_{oil} (eq) > ΔC_{wall} (eq)	No	Yes

One finds that, for both sets of the experiments, the increase in T_{oil} has caused the increases in T_{wall}. The changes in T_{wall} were less significant than those in T_{oil} for both studies. The major difference is that for the model oil, the gradient of its solubility curve (Figure 4) is virtually constant (i.e., the solubility curve is close to a straight line), so that the changes in $C_{oil}(eq)$ and $C_{wall}(eq)$ simply reflected the changes in T_{oil} and T_{wall}. These changes eventually lead to the increase in the mass driving force, $[C_{oil}$ (eq) - C_{wall} (eq)] and the characteristic mass flux, $J_{wax,c}$ for the model oil when T_{oil} increased. However, the gradient of the solubility curve for the North Sea Oil A decreased with increasing temperature (a concave solubility curve as shown in Figure 2), resulting in the changes in $C_{oil}(eq)$ and $C_{wall}(eq)$ to deviate from those from in T_{oil} and T_{wall}. Eventually, the change in $C_{wall}(eq)$ outweighs that in $C_{oil}(eq)$, thereby resulting in the increase of the driving force for the North Sea oil A. This analysis reveals that that mass driving force and thermal driving force do not necessarily share the same trend, and that the mass driving force could decrease with increasing thermal driving force if certain requirements are met. Appendix B provided further discussions to the conditions that could cause opposite

trends between mass driving force and thermal driving force. Moreover, this finding also demonstrates the advantage of using the mass driving force in comparison of the thermal driving force as it includes the impact of the solubility curve on wax deposition.

2.4.2. Comparison between the Carbon Number Distribution of the Model Oil and the North Sea Oil A

The above comparison has highlighted the importance of the shape of the solubility curve on the effects of the oil/coolant temperatures on wax deposition. The solubility of wax represents the multi-component solid-liquid equilibrium of the oil, which strongly depends on its carbon number distribution. Figure 9(a) shows the carbon number distributions of the C20+ components in the model oil used in Bidmus et al.[20], while Figure 9(b) shows the distribution for the North Sea Oil A used in this study. Two major differences can be observed between these two oils. First, a longer tail can be seen in the carbon number distribution of North Sea Oil A, indicating the existence of heavy paraffins (C50-C80), which are not existent in the model oil. In addition, lighter components (C20-C26) account for 41% of the wax in North Sea Oil A, while they only account for 26% of the wax in the model oil. The small amount of the heavy components and the excess amount of the light components in North Sea Oil A causes a greater precipitation of wax at lower temperatures compared to the model oil. This greater precipitation is consistent with the concave shape of the solubility curve of the North Sea Oil A at low temperatures and eventually explains the contradictory observed trends of growth of deposit thickness between Figures 6 and 8.

(a) Bidmus et al.[8] (Model Oil) (b) Current study (North Sea Oil A)
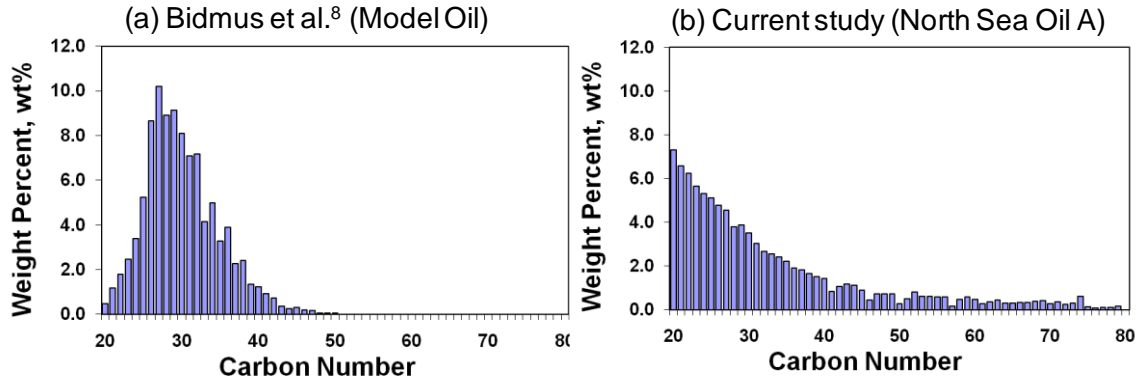
Figure 9: Carbon number distribution of the heavy components in (a) the model oil and (b) the North Sea Oil A

2.4.3. Method to Determine the Effect of Oil/Coolant Temperatures

Based on the analysis above, we have summarized the algorithm to indentify the change of the amount of wax deposition with changes in the oil/coolant temperatures as follows:

Step 1: Calculate the wall temperature at the beginning of the experiment where no wax deposit has yet formed on the wall. This can be done by either solving the heat transfer equation numerically or via the correlations that account for the heat transfer coefficients for the oil and the coolant.[23,24]

Step 2: Calculate the diffusivity of the wax in the oil at the wall temperature, $D_{wo, wall}$.

Step 3: On the basis of the solubility curve of the oil, calculate the equilibrium concentrations in the bulk and at the wall, C_{oil}(eq) and C_{wall}(eq), and thus the mass driving force [C_{oil}(eq) - C_{wall}(eq)].

Step 4: Calculate the characteristic mass flux for wax deposition, $J_{wax,c}$, as shown in Equation (10). Compare this parameter for experiments where the oil or the coolant temperatures are varied. The experiments with higher mass driving force should have a greater increase rate of deposit thickness.

2.5 Conclusions

In this study, an analysis was carried out using the Michigan Wax Predictor (MWP) to establish guidelines to determine the effect of the oil and the coolant temperatures on wax deposition thickness. The MWP was first applied to a series of flow loop deposition experiments, in which the oil temperature and the coolant temperature were all changed independently. It is found that the MWP successfully has predicted the effects of the operating conditions on wax deposition for North Sea Oil A without using any adjustable parameters. These effects include reduced deposition with increasing oil temperature and with increasing coolant temperature.

In the subsequent analysis using the MWP, the effect of the oil/coolant temperatures on wax deposition is seen in their impact on the characteristic mass flux for wax deposition, $J_{wax,c}$, which includes the diffusivity $\underline{D}_{wo,\,wall}$ and the mass driving force, $[C_{oil}\,(eq) - C_{wall}\,(eq)]$. The mass driving force for wax deposition is a more appropriate parameter to quantify the temperature effects on wax deposition in comparison to the thermal driving force $[\Delta T = (T_{oil} - T_{coolant})]$.[4,18,20]

It is found that the shape of the solubility curve can greatly affect the mass driving force by affecting the equilibrium concentrations of wax in the bulk oil and at the wall. The analysis is carried out by investigating the contradictory change in the deposit thickness between experiments using a North Sea Oil A and those using a model oil-wax solution. It was found that for the North Sea Oil A the amount of wax deposit decreases when the oil temperature increases, which is a trend that has not been observed in the study of the model oil-wax solution. By analyzing the parameters involved with the mass flux, $J_{wax,c} = \{D_{wo,\,wall}\,\{C_{oil}\,(eq) - C_{wall}\,(eq)]/r_i\}$, it is found that the difference in the shape

of the solubility curves between these two oils can be used to explain the difference in their experimental trends. The concave shape of the solubility curve of the North Sea Oil A results in a more drastic change in C_{wall}(eq) compared to C_{oil}(eq), while the linear shape of the solubility curve for the model oil-wax solution leads to a less significant change in C_{wall} (eq) in comparison to C_{oil}(eq). This difference in the changes in the equilibrium concentrations leads to the difference in the behavior of the mass driving force, which eventually explains the opposing trends in the amount of wax deposit observed in the their experiments when the oil temperature is varied. Furthermore, this discrepancy in these two oils' solubility curves is a result of the difference in their carbon number distributions. It should be noted that using model oils in the investigation of wax deposition can lead to misleading conclusions that are significantly different from those seen in the real crude oils.

CHAPTER 3

The Counterintuitive Explanation of Effects of Oil Flow Rate on Wax Deposition

3.1 Introduction

3.1.1. Background

The transportation of oil from the reservoir to the processing facilities has been a vital part in the production in the petroleum industry. As reservoirs close to the shore become depleted over time, the focus of production shifted toward reservoirs further away from the shore. As a result, the distance that crude oil is transported through the subsea pipelines is increased and a variety of issues related to flow assurance arise.[26-32] As the crude oil flows through the subsea pipelines resting on the ocean floor at $4°C$, the temperature of oil near the pipe wall decreases below its cloud-point temperature (i.e. wax appearance temperature, WAT) owing to its heat loss to the surroundings. As a result, the dissolved wax molecules precipitate out from the oil and form deposits on the cold pipe wall. This wax deposit is shown to have structures of thin platelets that overlap and interlock to form a gel, which has become one of the biggest challenges for the flow assurance of the petroleum fluids.[33] Significant increases in production costs result from the remediation techniques, such as pigging, pipeline insulation and heating. Insufficient

pigging frequency can result in a deposit that grows so thick that the pig has been known to get stuck, which stops the flow of petroleum fluids. However, too high of a pigging frequency can lead to additional costs of tens of millions of dollars due to deferred production. An estimate of these costs for different pigging frequencies for a 29-km long tieback is shown in Figure 10.[15]
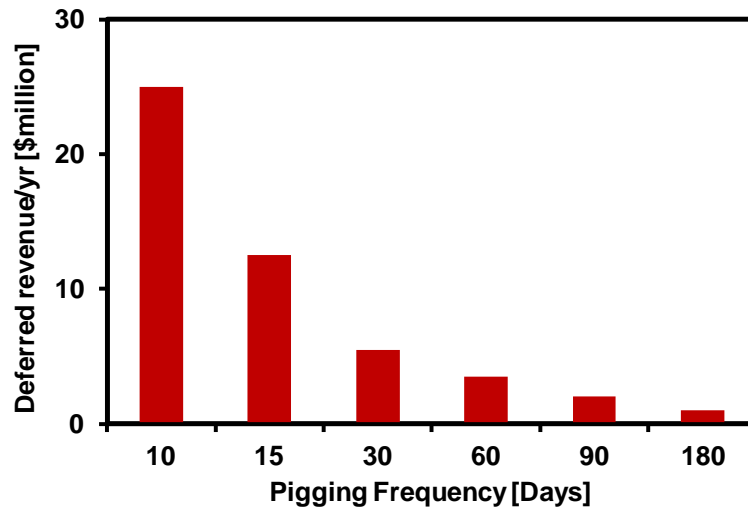
Figure 10: The cost of deferred production drops with pigging frequency[15]

Consequently, an understanding of the fundamental physics of wax deposition, especially its behavior under different operating conditions is important to design effective remediation strategies, such as pigging frequency.

3.1.2. Decreasing Wax Deposition with Increasing Oil Flow Rate

To study the wax deposition in the subsea pipelines, many lab-scale and pilot-scale experimental studies have been carried out at different oil flow rates. Jennings et al. used a coldfinger apparatus and a crude oil from the Gulf of Mexico to study wax deposition at different stirring speeds while the temperature difference between the crude oil and coldfinger surface was kept constant.[18] It was found that the experiments with higher stirring speeds yielded smaller amounts of deposit. Creek et al. observed similar trends

using a flow-loop apparatus to study wax deposition, namely increasing oil flow rates could substantially decrease wax deposition.[4] In the study by Tinsley et al., a channel flow apparatus was used to perform wax deposition experiments at three oil flow rates and it was found that the deposit thickness was reduced with increasing oil flow rates.[34] In all the above studies, an intuitive generalization was made that this trend of reduced deposit with increasing flow rates is due to the so-called "shear removal" mechanism. Here the terminology of "shear removal" referred either to the possible continuous retardation to the build-up of the deposit by the fluid at the oil-deposit interface or to the sloughing that causes the sudden removal of a layer of the deposit, especially in the flow regime with relatively high Reynolds numbers.[4,18,34] However, equally important is the role of heat and mass transfer when the flow rate is changing, which was frequently overlooked in previous studies. The change of flow rate alters the boundary layer thickness as well as the interface temperature, both of which further affect the diffusion of wax molecules into the interface and the rate of deposit thickness growth.

This influence of flow rate on heat and mass transfer was also mentioned in the studies by Merhotra et al. [35 - 38] However, these studies only analyzed the heat transfer characteristics to explain the effect of oil flow rate at the thermal pseudo-steady state, and did not analyze how heat and mass transfer and deposit thickness change with time. In the current work, a fundamental analysis is carried out from the first principles to elucidate the trend of reduced deposit thickness with increasing flow rate, especially focusing on how the effect of heat and mass transfer involves with time.

3.2 Wax Deposition Experiments

A series of experiments were carried out using a pilot-scale flow-loop in the Herøya Research Center of Statoil ASA in Porsgrunn, Norway to investigate the effect of oil flow rate on wax deposition. The flow-loop is equipped with a reservoir of 4 m^3 and a test section with a length of 5.5 m and an inner diameter of 5.3 cm. A crude oil from the North Sea with a wax content of 4.5%wt (identified as North Sea Oil A) is provided by Statoil ASA and is used in this study for deposition experiments. The detail information of flow-loop along with the characterization techniques to study wax deposition have been reported by Hoffmann and Amundsen.[21]

3.3 Single Phase Wax Deposition Modeling

Due to the fact that water and gas frequently accompany oil in flowing subsea pipelines, wax deposition will eventually need to be analyzed in multiphase flow conditions.[39] However, most of the existing wax deposition studies are limited in the scope to single-phase flow, where reliable transport correlations on the hydrodynamics are developed well.

Two major aspects are involved in wax deposition modeling in single phase: heat transfer and mass transfer. In the past twenty years, a series of studies have developed several wax deposition models from the different perspective of heat and mass transfer: [12,17,35-38,40,41] Merhotra et al. analyzed the heat transfer characteristic during the flow of oil through a pipeline and developed a model to predict wax deposition thickness at the thermal pseudo-steady state.[35-38] In these studies it is stated that the wax build is reached within twenty minutes in their 48mm-long, non-flow-loop apparatus. However, one should note that owing to the pipe insulation in field pipeline conditions and industrial

size flow loops, wax deposition normally occurs in a much longer time scale. For example, a pigging frequency of a threshold of 4mm deposit thickness can be on the order of days, weeks to months. Therefore, the conclusion obtained from their apparatus is not representative of the flow in the pipelines. In addition, as this model solely relies on heat transfer analysis without any mass transfer applications, it could only predict wax deposit thickness when the deposit stops growing and is unable to predict the build-up of wax deposit with time. Therefore the applicability of this model is limited.

A mathematical model (the Michigan Wax Predictor (MWP)) based on earlier studies of Singh, Venkatesan, Lee and Huang et al. was applied in the current study to investigate the oil flow rate effects on wax deposition.[12,17,40,41] The MWP applies the Graetz boundary conditions, and the flow of the oil is assumed to be in a quasi-steady state, while the wax thickness, δ, increases with time. The external heat transfer coefficient for the coolant was calculated using the correlation by Monrad and Pelton to account for the heat loss to the coolant flowing in the annuli of the pipe.[42] The internal heat and mass transfer rates were calculated using a 2D axial symmetry energy equation and the correlation for eddy diffusivity by Van Driest.[24] The model calculates the axial convection and the radial conduction/diffusion for the heat and mass transfer equations to determine the temperature profile as well as the concentration profile of wax molecules.[12]

With information of the concentration profile, the concentration gradient at the interface can be used to calculate the growth rate of both the deposit thickness and the wax fraction in the deposit, using molecular diffusion as the major mechanism for wax deposition. The details of this model can be found in the work of Lee and Huang et al.[12]

It should be noted that the equations in the model were developed from first principles and that no tuning parameters were used. In this analysis of mass transfer, it is assumed that wax molecules only precipitate at and in the deposit and that they do not precipitate in the oil phase.

This approach is similar to the one used in the laminar flow model by Singh et al., where the heat and mass transfer correlations were decoupled.[17] In addition, the model in the current study does not need to incorporate the so-called "shear removal" effect, that is, the detachment of the deposited wax material from the pipe wall by the flowing oil, to predict the observed trends. Because the effect of bulk precipitation and shear removal are highly empirical, the use of tuning parameters to include these effects can reduce the reliability for our conclusions and therefore not included. Consequently, the major focus of this model is to examine a number of deposition experiments in general to determine whether the model repeats the trends shown in the experiments rather than comparing each experiment with their corresponding model predictions.

3.4 Using MWP to Understand the Effects of Oil Flow Rate on Wax Deposition

3.4.1. Analyzing the Transport Terms

In order to understand the effect of oil flow rate on wax deposition, one has to first identify the most important parameters affecting wax deposition and investigate the effect of oil flow rate on each of these parameters. In the molecular diffusion mechanism, two mass fluxes of wax molecules contribute to the deposition process as shown in Figure 11:
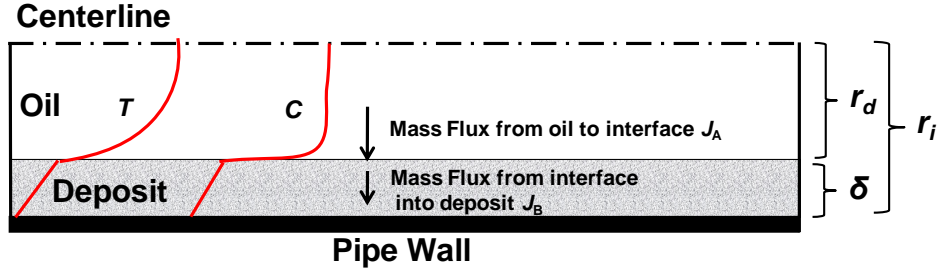
Growth of the deposit thickness = J_A - J_B

Growth of the wax fraction in the deposit = J_B

Figure 11: Sketch of molecular diffusion mechanism for wax deposition

(A) The mass flux from the bulk oil to the deposit interface, J_A;

(B) The mass flux from the interface into the deposit, J_B;

The mass flux into the deposit leads to the increase of the average wax fraction in the deposit, $\overline{F}_w$. Applying the quasi-steady state assumption in the boundary layer, $\overline{F}_w$ is given by Equation (11).

$$J_B = 2\pi r_d \left(-D_{\text{eff}} \left. \frac{dC}{dr} \right|_{\text{from interface into deposit}} \right) = \pi \rho_{\text{dep}} \left(r_i^2 - r_d^2 \right) \frac{d\overline{F}_w}{dt} \tag{11}$$

The difference between the mass flux from the bulk to the interface and the mass flux into the deposit corresponds to the growth of the deposit thickness, δ, and is given by Equation (12).

$$J_A - J_B = 2\pi r_d \left(-D_{\text{wo, interface}} \left. \frac{dC}{dr} \right|_{\text{from oil to interface}} \right) - 2\pi r_d \left(-D_{\text{eff, interface}} \left. \frac{dC}{dr} \right|_{\text{from interface into deposit}} \right) = 2\pi r_d \rho_{\text{dep}} \overline{F}_w \frac{d\delta}{dt} \tag{12}$$

These two mass balance equations are used in the Michigan Wax Predictor (MWP) to predict the increase in both the thickness and the wax fraction of the deposit.

In the current study, the mass flux from the bulk oil to the deposit interface (the first term in parentheses in the middle of Equation (12)) was found to be significantly greater

than the diffusive mass flux into the deposit (the second term in the middle of Equation (12)) due to the enhanced radial mass transfer in the oil phase by the movement of the fluid. Therefore, we can approximate the growth rate of wax deposit as being essentially equal to the mass flux of wax molecules from the bulk to the interface, J_{wax}. With this assumption Equation (12) reduces to:

$$\rho_{\text{dep}} r_{\text{d}} \bar{F}_{\text{w}} \frac{d\delta}{dt} = \underbrace{J_{wax} \approx D_{\text{wo, interface}}}_{\textbf{Term 1}} \underbrace{\left(-\frac{dC}{d(r/r_{\text{d}})}\bigg|_{\text{from oil into interface}} \right)}_{\textbf{Term 2}} \qquad (13)$$

The RHS of Equation (13) contains the most important parameters for the wax deposition and will be used in this study to analyze the effect of oil flow rate on wax deposition. For ease of explanation, the RHS of Equation (13) is further divided into Term 1 and Term 2.

3.4.2. Theoretical Analysis of the Effect of Oil Flow Rate on Wax Deposition

To understand the counterintuitive effects of oil flow rate on wax deposition, one can analyze the effects of the oil flow rate on the two terms shown in Equation (13) separately, i.e. Term 1: the diffusivity at the oil-deposit interface, $D_{\text{wo, interface}}$ and Term 2: a radial concentration gradient at the interface in the form of $\dfrac{\partial C}{\partial(r/r_{\text{d}})}$.

3.4.3. Factors Affecting the Concentration Gradient

Theoretical insights into the concentration gradient, $\dfrac{\partial C}{\partial(r/r_{\text{d}})}$ (Term 2 in Equation (13)) can be obtained by analyzing the "Graetz Problem" for mass transfer where convection is prevalent in the axial direction and diffusion in the radial direction.[43] The mass balance equation in the "Graetz Problem" is also used in the MWP to determine the concentration profile of wax molecules, as shown in Equation (14).

37

$$V\frac{\partial C}{\partial z} = \frac{1}{r}\frac{\partial}{\partial r}\left((D_{wo} + \varepsilon_{mass})r\frac{\partial C}{\partial r}\right) \tag{14}$$

The corresponding boundary conditions are shown in Equation (15).

$$\begin{cases} \text{at } z = 0,\ C = C_{inlet} \\ \text{at } r = 0,\ \dfrac{\partial C}{\partial r} = 0 \\ \text{at } r = r_d,\ C = C_{interface} \end{cases} \tag{15}$$

Analysis of the radial concentration profile provides basic understanding of the elements that affect the concentration gradient $\dfrac{\partial C}{\partial(r/r_d)}$ (Term 2 in Equation (13)). The analysis includes the following two effects.

First, an increase in the oil velocity, V_{oil} (i.e. a corresponding increase in the oil volumetric flow rate, Q_{oil}) generates a smaller boundary layer and a steeper radial concentration profile, resulting in an increase in $\dfrac{\partial C}{\partial(r/r_d)}$ as shown in Figure 12.
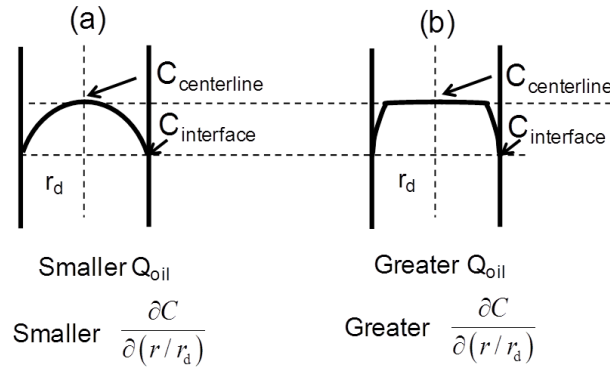
Figure 12: Sketches of the concentration profiles with different Q_{oil}

Secondly, both sides of Equation (14) can be de-dimensionalized as shown in Equation (16).

$$v\frac{\partial\theta}{\partial\lambda}=\frac{1}{\eta}\frac{\partial}{\partial\eta}\left[\frac{4}{\text{Gz}}\eta\frac{\partial\theta}{\partial\eta}\right]$$

$$\text{where }\left(\theta=\frac{C-C_{\text{interface}}}{C_{\text{inlet}}-C_{\text{interface}}}\right),\left(v=\frac{V}{U}\right),\left(\lambda=\frac{z}{L}\right),\left(\eta=\frac{r}{r_{\text{d}}}\right),\left(\text{Gz}=\frac{d_{\text{d}}^{2}U}{L(D_{\text{wo}}+\varepsilon_{\text{mass}})}\right)$$

(16)

Based on Equation (16), one notes that the de-dimensinalized concentration gradient,

$\dfrac{\partial\theta}{\partial(r/r_{\text{d}})}$ is independent of the difference between the two boundary concentrations,

($C_{\text{centerline}}$ - $C_{\text{interface}}$). Therefore, the concentration gradient, $\dfrac{\partial C}{\partial(r/r_{\text{d}})}$ can be found to be

directly proportional to $\left(C_{\text{centerline}}-C_{\text{interface}}\right)$, as given by Equation (17).

$$\frac{\partial C}{\partial(r/r_{\text{d}})}=\frac{\partial C}{\partial\theta}\frac{\partial\theta}{\partial(r/r_{\text{d}})}=\left(C_{\text{centerline}}-C_{\text{interface}}\right)\frac{\partial\theta}{\partial(r/r_{\text{d}})}$$

(17)

Because of the short experimental test section length of the pipe in the flow loop

apparatus (5.5m), no significant axial variations were observed (i.e., less than 2%) for the

fluid properties. Consequently, $C_{\text{centerline}}$ is essentially the same as both C_{inlet} and C_{oil},

which is the concentration of the wax in the bulk oil. In order to avoid potential confusion,

only C_{oil} will be used for the subsequent quantitative analyses.

3.4.4. Counterintuitive Explanation of the Effects of Oil Flow Rate on Wax Deposition

The above discussion has provided insights on the factors affecting the gradient

$\dfrac{\partial C}{\partial(r/r_{\text{d}})}$ (Term 2 in Equation (13)). In terms of the diffusivity at the oil-deposit interface,

$D_{\text{wo, interface}}$ (Term 1 in Equation (13)), a change in the oil flow rate can result in the

change in the interface temperature, $T_{\text{interface}}$, thereby altering $D_{\text{wo, interface}}$. In summary, an

increase in Q_{oil} can produce several competing effects, which either increase or decrease

the mass flux from the bulk to the interface, J_{wax}, which is governed by Equation (18):

$$J_{wax} \approx \underbrace{D_{wo,\,interface}}_{\text{Term 1}} \underbrace{\left(-\frac{dC}{d(r/r_{\mathrm{d}})}\bigg|_{\text{from oil into interface}} \right)}_{\text{Term 2}} \qquad (18)$$

Effect 1: An increase in Q_{oil} tends to provide a smaller boundary layer and a steeper radial concentration profile, thereby increasing $\dfrac{\partial C}{\partial(r/r_{\mathrm{d}})}$ and thus increasing the mass flux, J_{wax} as given in Equation (18);

Effect 2: An increase in Q_{oil} causes more hot oil to be pumped through the pipe and thus leads to an increase in $T_{interface}$. This increase in the interfacial temperature causes the diffusivity at the interface, $D_{wo,\,interface}$ to increase, thereby increasing the mass flux, J_{wax};

Effect 3: An increase in Q_{oil} results in an increase in $T_{interface}$, which leads to a higher concentration of dissolved wax molecules at the interface, $C_{interface}$, as can be seen in the solubility curve shown in Figure 13. The solubility curve of the wax in the oil is *the* most influential input parameter for the deposition model and has been experimentally determined by Han et. al.[22]
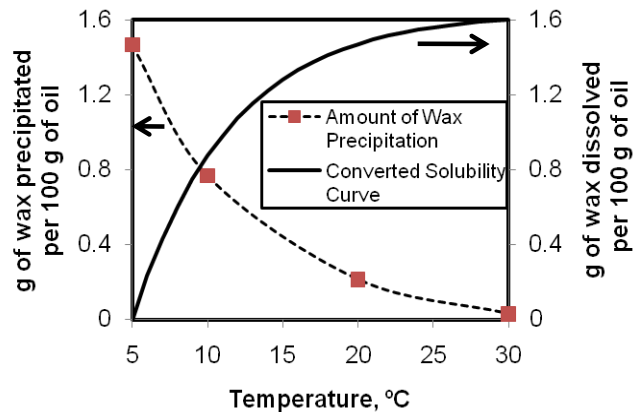
Figure 13: The amount of precipitation of wax in oil at various temperatures and the corresponding solubility curve for the North Oil A.[22]

This increase in $C_{\text{interface}}$ decreases the concentration difference (C_{inlet} - $C_{\text{interface}}$), thus decreasing the gradient $\dfrac{\partial C}{\partial (r/r_{\text{d}})}$ and thus the mass flux, J_{wax}, as shown in Equation (18);

In most deposition problems occurring at isothermal conditions, a faster deposition rate is observed with increasing flow rate because only **Effect 1** plays a role in affecting the radial mass flux. However, in the case of wax deposition, which occurs under non-isothermal conditions, the existence of **Effects 2 and 3** delineates how the interaction of heat transfer and the solubility curve can alter the conclusions from isothermal conditions, which can result in the counterintuitive effects of flow rate on the wax deposition rate. More specifically, **Effects 2 and 3** involve the behavior of $T_{\text{interface}}$, which can change with time due to the increase in the insulation thickness as the deposit builds up on the wall. Therefore the dynamics of the competition between all three of these effects can vary as time progresses. Consequently, the comparison of the three effects at different times is necessary to thoroughly understand the effect of the oil flow rate on wax deposition.

3.5 Results and Discussions

3.5.1. Flow-loop Results and Predictions of the Experimental Trends by MWP

In order to investigate the effect of oil flow rate on wax deposition, five experiments with different oil flow rates were conducted in the pilot-scale flow-loop apparatus and the corresponding thicknesses were predicted by MWP. The operating conditions of these five experiments are summarized in Table 5.

Table 5: Summary of the operating conditions in the pilot-scale flow-loop experiments

Parameters	Value				
T_{oil}, ^{0}C	20.0				
$T_{coolant}$, ^{0}C	10.0				
Q_{oil}, m^3/h	5.0	10.0	15.0	21.0	25.0
Re	9942	19884	29826	41756	49710
τ_{wall}, Pa	1.93	6.06	11.62	19.45	26.64

Figure 14 shows the experimental and theoretical trajectories of wax thickness as a function of time for different oil flow rates.
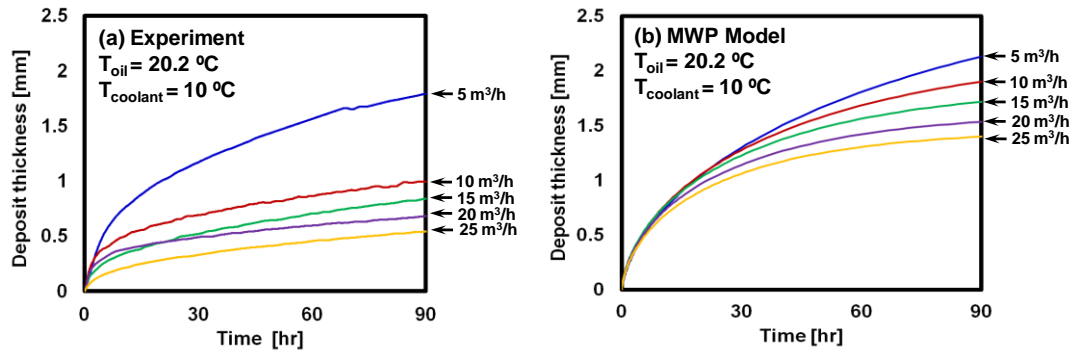
Figure 14: Comparison of deposit thickness as a function of oil flow rate, Q_{oil} between (a) the experimental results[21] and (b) the model prediction by the MWP. The oil temperature, T_{oil}, was maintained constant at 20 ℃ and the coolant temperature, T$_{coolant}$ was maintained at 10 ℃

It should be noted that the focus of Figure 14 is to compare the trend of deposit thicknesses for different oil flow rates at later times because the conversion of pressure drop measurements to thicknesses is much more reliable during this time periods compared to the early stages. In the early stages of deposition, the deposit accumulation at this stage is close to zero and not easily captured by the pressure drop measurement. Consequently, the experimental error in the growth of the wax deposit is relatively larger because of the sensitivity and uncertainty of the measuring instrument to small changes in pressure drop.

As can be seen in Figure 14, both the experiments and model predictions reveal that the deposit thickness decreases with increasing oil flow rate, which is the same trend as observed in other wax studies. In addition, one also notes that the difference in the thickness profiles between the different flow rates increases with time: while at the beginning of the experiments, the thicknesses for different flow rates are similar, as time progress a greater difference in the deposit thickness is observed for different flow rates. This change in the sensitivity of thickness to Q_{oil} at different times indicates the dynamics of the competition among these three effects changes with time. Because of the agreement of the trends between the experiments and the predictions by the MWP at later times in Figure 14, the MWP will be applied to analyze and explain the results shown in this study.

3.5.2. Analysis of the Dynamics of Three Effects

3.5.2.1. Comparison of Three Effects Initially

In order to weight the impact of these three effects, the initial (i.e. $t=0^+$) mass fluxes from the oil towards the deposit, J_{wax} for different Q_{oil} are compared and the results are shown in Figure 15:
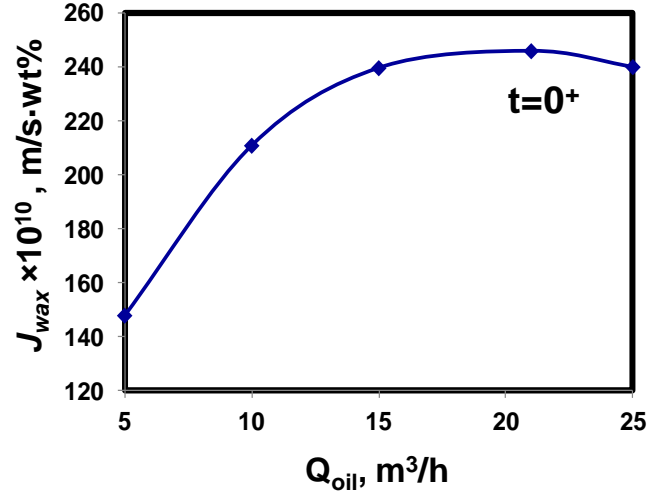
Figure 15: Comparison of J_{wax} at t=0[+]

It can be seen from Figure 15 that at $t = 0^+$, J_{wax} does not exhibit a monotonic trend with respect to Q_{oil} (it increases from 5m³/h to 21m³/h and slightly decreases from 21m³/h to 25m³/h). This non-monotonic trend indicates that when Q_{oil} changes from 5m³/h to 21m³/h, the combination of **Effects 1** and **2** dominates to increase J_{wax} and hence the deposit thickness. However between Q_{oil}=21m³/h and 25m³/h, **Effect 3** is more dominant thereby leading to a reduction in the mass flux, J_{wax} and thus the deposit thickness. Initially, these three effects are comparable, but at later times as the wax builds up, **Effect 3** dominates the other two, which will be discussed later.

3.5.2.2. Change in the Dominance of Effects 2 and 3 with Time

As mentioned previously, the strength of **Effect 1** is independent of time but the strengths of **Effects 2 and 3** change as time progresses as they involve the behavior of $T_{interface}$, which increases with time due to the insulating effect from the build-up of the wax thickness on the wall. In order to compare the dynamics of three effects at different times, the change in the strengths of **Effects 2 and 3** with time must be first clarified.

44

A quantitative comparison of **Effect 2** with time can be found from the diffusivity ratio, R_D, which is the ratio of the diffusivity at the interface for given oil flow rate, $Q_{oil} = Q_i$, i=5, 10, 15 ,21, 25m^3/h to the value of the diffusivity at the interface when $Q_{oil} = 5$m^3/h, as shown in Equation (19):

$$R_D = \frac{D_{\text{wo, interface, Q=i}}}{D_{\text{wo, interface, Q=5m}^3\text{/h}}} \quad \text{where i=5, 10, 15 ,21, 25m}^3\text{/h} \tag{19}$$

A sketch of this ratio as a function of Q_{oil} is shown as Figure 16. Because an increase in Q_{oil} leads to an increase in $T_{\text{interface}}$, which causes $D_{\text{wo, interface}}$ to increase and thereby increasing the mass flux, the slope of the ratio as a function of Q_{oil} is greater than zero. The value of the slope represents the strength of **Effect 2** and one can investigate the change of **Effect 2** with time by comparing the slope at different times.

A similar approach can be used to investigate the change of **Effect 3** with time. In this case, the concentration ratio, R_C, which is the ratio of concentration difference between the bulk and interface at a given oil flow rate, $Q_{oil} = Q_i$, i=5, 10, 15 ,21, 25m^3/h to the concentration difference when $Q_{oil} = 5$m^3/h, is used as the indicator, as shown in Equation (20).

$$R_C = \frac{\left(C_{\text{oil}} - C_{\text{interface}}\right)\big|_{Q_{oil}=i}}{\left(C_{\text{oil}} - C_{\text{interface}}\right)\big|_{Q_{oil}=5m^3/h}} \quad \text{where i=5, 10, 15 ,21, 25m}^3\text{/h} \tag{20}$$

Because Effect 3 tends to decrease the driving force and thus the J_{wax}, the deposit thickness decreases as Q_{oil} increases. Consequently, the slope of a plot of R_C as a function of Q_{oil} is less than zero.
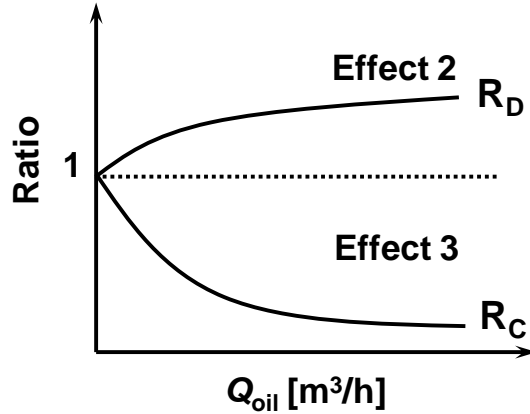
Figure 16: Qualitative sketch of the indicators of the time dependency of **Effect 2 and Effect 3**

The values of R_D and R_C at different times are calculated by the MWP and summarized in Figure 17 (a) and (b) respectively.
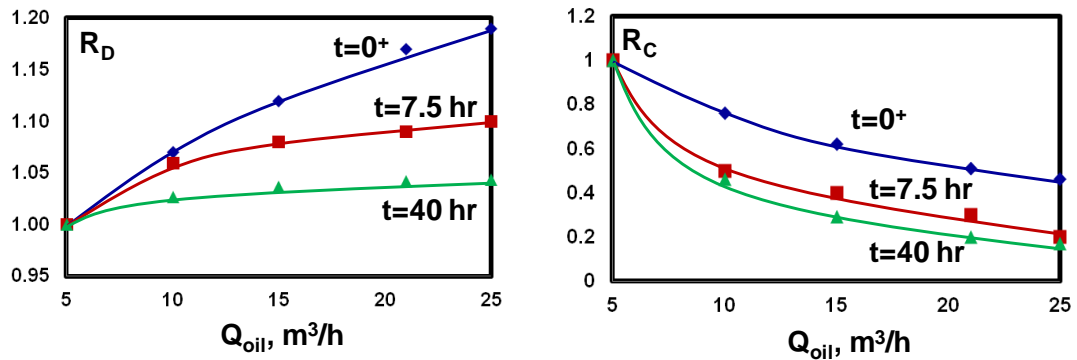
Figure 17: Quantitative representation of the change of Effects 2 and 3 with time

By comparing the diffusivity ratio, R_D at different times one can see that as Q_{oil} increases from 5m³/h to 25m³/h, R_D has increased 19% at t=0, but only increased 10% at t=7.5 hours. This difference in the increment of R_D between t=0 to t=7.5 hours indicates that **Effect 2** has weakened as time progresses. Similarly, by comparing the concentration difference ratio, R_C between t=0 and t=7.5 hours, one can see that **Effect 3** has strengthened with time.

The summary of the dynamics of these three effects are listed in

Table 6.

Table 6: Summary of the involvement of three effects as time progresses

	Effect 1	**Effect 2**	**Effect 3**
t=0	Similar magnitude as no monotonic trend with increasing Q_{oil} is shown		
Time progresses	No change	Weakens	Strengthens

It can be seen that although initially none of these three effects dominates with increasing Q_{oil}, **Effect 3** strengthens as time progresses and eventually dominates the other two effects. This domination causes the wax deposition to decrease with increasing Q_{oil} and provides important insights to the counterintuitive effects of oil flow rate on wax deposition.

3.6 Closing Comments

The above discussions have shown that the heat and mass transfer effects can be used to explain the counterintuitive effects of flow rate on deposition. It should be noted that several studies also proposed the so-called "shear removal" mechanism, which referred either to the possible continuous retardation to the build-up of the deposit by the fluid at the oil-deposit interface or to the sloughing that causes the sudden removal of a layer of the deposit, especially in the flow regime with relatively high Reynolds numbers.[4,18,34] In those studies, a form of mass flux, $J_{removal}$ is proposed to represent this removal of wax from the wall due to shear. However, a fundamental mechanism describing this removal flux, $J_{removal}$ has not yet been made and the existing models are still highly empirical.[2] Consequently, the outlook of this study is to provide an alternative explanation for the reduced deposit thickness with increasing flow rate from the perspectives of heat and mass transfer. The future outlook of this research is to compare the heat and mass transfer

47

effects and the effect of potential "shear removal" in order to identify the major reason for the effects of the flow rate on wax deposition.

3.7 Conclusions

In this study, the Michigan Wax Predictor (MWP) builds on a number of previous Ph.D. theses at the University of Michigan was applied to elucidate using first principles the experimental trend of reduced deposit thickness with increasing flow rate. Despite the fact that many previous studies intuitively attribute the reason to the "shear removal", this study has indentified three effects that give rise to an alternative explanation, which has been overlooked in previous studies. It was found that these three effects include the effect of the boundary layer thickness on mass transfer (**Effect 1**), the diffusivity at the interface on mass transfer (**Effect 2**) and the interface wax concentration on mass transfer (**Effect 3**). Both **Effects 1 and 2** tend to increase the growth rate of the wax deposit while **Effect 3** tends to have the opposite effect. The overall growth behavior of the wax deposit is the result of the competition between these three effects.

More importantly, the dynamics of the competition between these three effects vary as time progresses. It was found that **Effect 1** changes insignificantly with time, while **Effect 2** weakens with time and **Effect 3** strengthens as time increases due to the insulation effect by the build-up of the wax deposit on the wall. Therefore while at the beginning of a wax deposition experiment these three effects are shown to be comparable of each other, **Effect 3** eventually dominates the competition over the other two, which explains the experimental trends observed in the flow loop apparatus that the reduced deposition with increasing flow rate.

CHAPTER 4

Fatty Acids for Nutraceuticals and Biofuels from Hydrothermal Carbonization of Microalgae

4.1 Introduction

Microalgae, which are photosynthetic single-celled organisms that reside in both marine and fresh water environments, are an attractive renewable feedstock for nutraceuticals and biofuels production, because of their fast growth rate, the ability to use nonarable land for their cultivation, and the diverse lipid contents and composition they can contain.[11, 44-47] Microalgae contain various types of lipids, among which fatty acids attract the primary interest. The majority of these fatty acids exist as triglycerides stored in the cell chloroplasts, but they also exist as glycolipids and phospholipids.[48] The common process for recovering algal lipids involves their extraction from the biomass and the subsequent conversion of the extracted lipids to products. Developing an effective, environmentally responsible, and economically viable extraction procedure is vital to ensure the success of subsequent processing steps and the sustainability of the entire production procedure.[11]

The two lipid-extraction techniques that have received the most attention to date use either liquid solvents or supercritical fluid solvents.[49] Exposing the microalgal biomass to

a liquid solvent, typically a petroleum-derived organic liquid, extracts lipids out of cellular matrices. A variety of solvent systems, including hexane, ethanol, chloroform/methanol/water, butanol, and ionic liquids have been investigated.[50 - 52] Among these solvent systems, the combination of chloroform, methanol, and water, also known as the Bligh and Dyer solvent system, has been shown to be effective for extracting lipids from microalgae and is commonly used as a standard for comparison of the efficiency of different solvent extraction systems.[46] However, the use of chloroform in large quantities for food and cosmetic production is prohibited, because of its carcinogenicity and health hazard to animals and humans.[53]

Another technique explored for extracting microalgal lipids is supercritical fluid extraction.[54-55] CO_2 is, by far, the most common supercritical fluid used for microalgal lipid extraction, because it is nonflammable, nontoxic, inexpensive, and chemically inert. Moreover, the moderate critical temperature (i.e., 31.1 °C) of CO_2 enables the intact extraction of thermally labile polyunsaturated fatty acids. The major disadvantage of supercritical fluid extraction is the higher cost of infrastructure and operation.[54]

Both solvent extraction and supercritical fluid extraction work best when the algal biomass has first been dried. The presence of water tends to reduce the contact between the extraction solvents and biomass, thus hindering the extraction process. Algal biomass, however, usually contains ~80% moisture even after mechanical dewatering, thus necessitating an algae drying process before the oil extraction step is attempted. The energy associated with vaporizing the water in and with the biomass is significant and must be minimized in a commercial process.[45] One way to avoid drying the algal biomass is to perform lipid extraction on the wet material. This approach has been examined, and

the extraction efficiency is typically reduced relative to what can be accomplished with dry biomass. For example, hexane extraction from a 30 wt% biomass wet algal paste resulted in 33% less lipid yield than from the corresponding dried biomass.[54]

Hydrothermal treatment refers to the process of subjecting a wet algal slurry to elevated temperatures and to pressures above the saturation pressure so that the water remains in the liquid phase. Since a liquid-vapor phase transition is avoided, hydrothermal treatment can be a more energy-efficient process than drying.[45] Hydrothermally treating wet algal biomass at mild temperatures (< 250 ℃) can produce a carbonized solid, or hydrochar, which retains a large fraction of the carbon and lipids in the original biomass. This process is often referred to as hydrothermal carbonization, or HTC. Unlike the original algae cells, the solid hydrochar particles formed by HTC are easy to separate from water by filtration.[56-58]

Garcia Alba *et al.* examined the morphology of algae cells after HTC at various temperatures, and they found that HTC was able to decompose the cell wall to release the intracellular compounds.[59] A different investigation revealed that the hydrochar was formed primarily through dehydration, condensation, polymerization, and aromatization of polysaccharides and proteins. Lipids contributed little to hydrochar formation, but were likely to be adsorbed along the tortuous surface of hydrochar structure.[60] Levine *et al.* used HTC as an initial step for making biodiesel from wet algal biomass and showed that the lipids retained in the hydrochar could be directly transesterified to crude biodiesel via uncatalyzed reactions with supercritical ethanol.[56] The temperatures (~275 ℃) required for this supercritical transesterification, however, likely caused decomposition of any high-value omega-3 fatty acids (e.g., eicosapentaenoic acid) that might have been

present. If one desires to recover polyunsaturated fatty acids from the hydrochar as a high-value coproduct stream, such elevated temperatures cannot be used. Rather, the retained lipids will need to be extracted from the hydrochar intact and then fractionated. Extracting lipids from the hydrochar, which is a solid-liquid extraction, should be much simpler than extracting them directly from wet algal biomass, where the presence of water would create a solid-liquid-liquid system that can lead to emulsification and liquid-liquid phase separation difficulties.

The extraction of lipids from hydrochar has received just limited prior attention. Heilmann *et al.* used methyl t-butyl ether (MTBE) to extract both the hydrochars and aqueous phases generated after HTC of three different algae at 200 ℃ and 2 h. The combined extracts contained most of the fatty acids in the original biomass.[61] More recently, the hydrochars and aqueous phases generated by HTC between 160 and 250 ℃ and from 15 min to 30 min were extracted for lipids using hexane. A maximum total fatty acid recovery of 70% was achieved.[62] These results demonstrate the possibility of recovering lipids and fatty acids from microalgae using an HTC-extraction approach; however, both studies used petroleum-derived solvents and focused on biofuel production. There has been no prior work with a renewable, food-grade solvent (e.g., ethanol), nor has there been prior work focused on recovery of high-value fatty acids (e.g., eicosapentaenoic acid) as a biorefinery coproduct. In addition, no information is available regarding the recoveries of specific individual fatty acid components in the HTC-extraction process at different HTC conditions. These gaps in the literature motivated the present work, in which we apply HTC as a pretreatment method for extracting fatty acids,

especially polyunsaturated fatty acids, from microalgae, using a food-grade solvent such as ethanol.

4.2 Methods

4.2.1. Materials

A 21 wt.% microalgal slurry of *Nannochloropsis sp.* provided by Valicor Renewables was the feedstock in this study. This algae species was selectively cultivated to be rich in palmitic acid (i.e., C16:0), palmitoleic acid (i.e., C16:1*n*-7), and eicosapentaenoic acid (EPA, i.e., C20:5*n*-3). The saturated palmitic acid (i.e., C16:0) is suitable for conversion to biodiesel or green diesel. As demonstrated by several clinical studies, the palmitoleic acid (i.e., C16:1*n*-7), an omega-7 fatty acid, and EPA (i.e., C20:5*n*-3), an omega-3 fatty acid, have a variety of health benefits against cardiovascular and inflammatory diseases.[63] Accordingly, the algae species studied in this work can be potentially used for both biofuels and nutraceuticals production. The total fatty acid content was determined to be 8.8% as fatty acid methyl esters (FAMEs) on a dry weight basis using the method described in Section 2.D.

Table 7 shows the fatty acid composition. EPA and palmitoleic acid accounted for ~60% of the total mass of fatty acids. The microalgal slurry was diluted to 15 wt.% with deionized water, homogenized, and stored at -4 ℃ prior to use.

Table 7: Fatty acid composition of *Nannochloropsis sp.* biomass

Fatty acid[*]	% of total fatty acids
C14:0	5.6
C16:0	16.5
C16:1*n*-7	18.3
C18:0	1.3
C18:1*n*-7	3.9
C18:1*n*-9	2.1
C18:2*n*-6	4.9
C18:3*n*-3	0.7
C20:4*n*-6	5.9
C20:5*n*-3	40.9
Total saturated fatty acids	23.3
Total monounsaturated fatty acids	24.3
Total polyunsaturated fatty acids	52.4

[*] Note: We use the omega notation system for fatty acids.[64] The first number is the total number of carbon atoms in the chain. The number following the colon is the number of double bonds in the chain, and the number following *n*- is the location (carbon atom number) of the first double bond.

All chemicals used in this work (i.e., anhydrous ethanol, methanol, acetyl chloride, and tricosanoic methyl ester) were analytical grade and obtained commercially. FAMEs standards were purchased from Nu-Chek Prep, Inc. Mini-batch reactors with an internal volume of ~4.1 mL were assembled from 316 Stainless Steel Swagelok parts (2 caps and 1 port connector).

4.2.2. HTC Procedure

Approximately 3 g of the homogenized 15 wt.% microalgal slurry was loaded into each reactor. The reaction was conducted by immersing sealed reactors in a preheated, isothermal fluidized sand bath for the desired amount of time and then quickly removed and cooled in water. We examined carbonization temperatures between 180 °C and 220 °C and reaction times from 15 min to 30 min. These hydrothermal reaction conditions were selected to provide sufficient cell conglomeration and disruption while minimizing the deterioration of unsaturated fatty acids during the HTC treatment. Upon

cooling, the reactor contents were emptied into a 50-mL centrifuge tube and then centrifuged (4000 RCF × 5 min) to separate the hydrochar and aqueous phase. The hydrochar was collected and kept in an oven at 65 ℃ until it had been completely dried.

4.2.3. Lipid Extraction

The dried hydrochar was subjected to batchwise solvent extraction with vigorous stirring. We used food-grade ethanol as the extraction solvent. Ethanol is available as a non-petroleum-derived solvent and is considered by the Food and Drug Administration to be less toxic than hexane for use in food applications.[65] In a typical experiment, 0.1 g of dried hydrochar was extracted by 3 mL anhydrous ethanol in a glass tube (16 mm × 100 mm) with Teflon-lined screw caps at 60 ℃ for 1 h with constant agitation via a magnetic stirrer (i.e., 500 rpm). After the desired time had elapsed, the solid-liquid mixture was centrifuged (2000 RCF × 5 min) and the ethanol phase was collected. The hydrochar debris was then extracted with another 3 mL aliquot of fresh anhydrous ethanol under the same conditions. Both extracts were then combined and transferred into a new, preweighed glass tube. The ethanol was evaporated in flowing N_2, and the lipid extract mass was quantified gravimetrically.

4.2.4. Fatty Acid Quantification

For their quantitative analysis, the fatty acid constituents of the lipids in the algal biomass, hydrochar, and lipid extract were catalytically transesterified to FAMEs. About 50 mg analyte was weighed into glass tubes (16 mm × 100 mm) with Teflon-lined screw caps and reacted with 2 mL of freshly prepared methanol (99%) containing 5% acetyl chloride as the acid catalyst at 100 ℃ for 90 min with vigorous stirring. When the reaction time had elapsed, 1 mL of water was added to the glass tube and the FAMEs

were extracted into 3 mL of n-heptane containing 250 mg/L tricosanoic methyl ester as an internal standard. This internal standard approach was adopted to improve the accuracy of quantification relative to direct area comparisons.[66] The tubes were vortexed for 2 min and then centrifuged (2000 RCF $\times$ 10 min). Approximately 2 mL of the upper heptane-FAME layer was transferred to a GC-vial and stored at 4 ℃ prior to analysis.

The amount of FAMEs in the sample was quantified by Agilent Model 7890A gas chromatography device using a flame ionization detector. A 1 μL sample was injected onto the J&W 1909BD-113 column (30 m $\times$ 0.32 mm $\times$ 0.25 μm) at a 10:1 pulsed split ratio. The oven temperature was initially at 150 ℃. After a 3 min hold, the temperature was ramped at 6 ℃ min^{-1} to 260 ℃. Helium was the carrier gas at a constant flow rate of 1.0 mL min^{-1}. The FID detector temperature was maintained at 300 ℃ and N_2 served as the makeup gas. FAMEs were identified based on retention time using a C_{14}-C_{24} standard FAME mix.

4.3 Results and Discussion

This section first provides the yield of hydrochar and fatty acids from HTC under different conditions. We then assess the ability of warm ethanol to extract these fatty acids from the hydrochar. The section concludes with a discussion of the results, their significance to the field, and a conceptual process flow diagram showing how this approach can recover algae oil containing both nutraceuticals and biofuels precursors.

4.3.1. Hydrothermal Carbonization
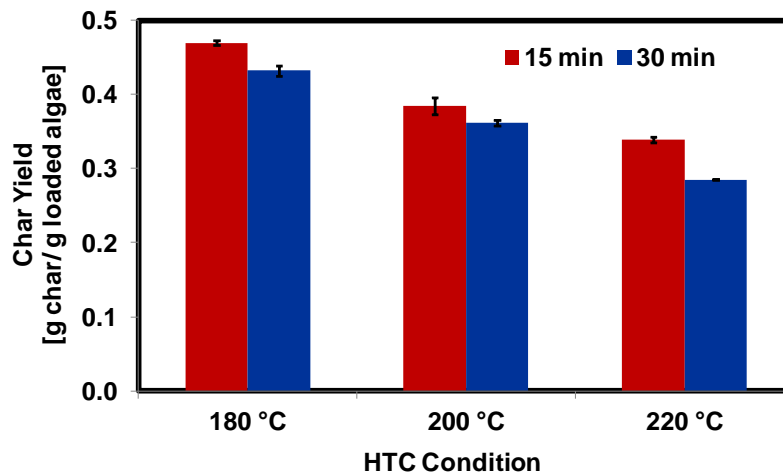
Figure 18: Hydrochar yields from HTC of *Nannochloropsis sp*. The error bars represent the standard deviation from replicate experiments.

HTC of the *Nannochloropsis sp*. biomass conglomerated it into a black and coal-like hydrochar. Figure 18 shows that the dry hydrochar yields obtained under different HTC conditions were between 30 and 47 % of the loaded algae mass, comparing favorably to the hydrochar yields reported for similar microalgae carbonization experiments around 200 ℃.[57-58] This magnitude of hydrochar yield implies that HTC converted more than half of the algal biomass into material that was released into the aqueous phase. Figure 18 also shows that for a given temperature, the longer carbonization time always produced a lower hydrochar yield and that for a given time, higher temperatures always produced lower hydrochar yields. The same trends were also observed in previous work.[58] We suspect that the lower char yields at more severe conditions is likely a result of increased hydrolysis of biomass constituents with increased reaction severity, which renders more of the material water soluble.
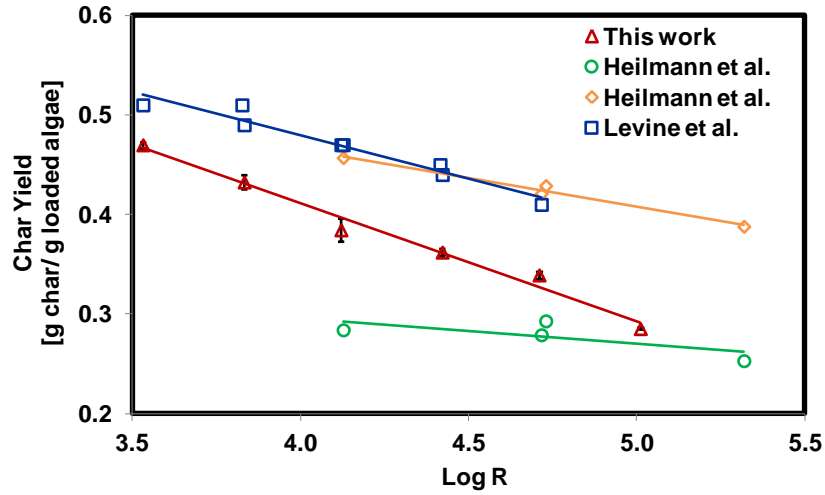
Figure 19: Hydrochar yields from HTC of microalgae under different carbonization conditions.

To facilitate a more quantitative comparison of the hydrochar yields obtained under different carbonization conditions, we offer Figure 19, which plots the hydrochar yield against the decimal logarithm of the reaction ordinate, R, defined as Equation (21).[67]

$$R = \int_0^t e^{\left(T(t)^\circ C - 100^\circ C\right) / 14.75^\circ C} dt \tag{21}$$

This quantity combines the effects of both carbonization time and temperature into a single parameter that expresses the overall reaction severity. It was previously shown to be a useful parameter for correlating results from hydrothermal liquefaction of microalgae.[68] Figure 19 also shows hydrochar yields reported for similar microalgae carbonization experiments.[57-58] These previous studies used different algae species and different biomass loadings (i.e., wt% algae in the slurry). Nevertheless, these data all suggest that a linear relationship exists between the hydrochar yield and log R for HTC of microalgae between 180 and 220 ℃ and from 15 to 120 min, independent of the types of algae species and the concentration of loaded biomass. To the best of our knowledge, this is the first report on this general trend for microalgae carbonization. This linear trend provides an opportunity to predict the char yield under conditions that have not been

58

explored experimentally. Such a capability can be useful for preliminary process design work. Also, the linear trend indicates that the fundamental behavior of different algae species during carbonization might be similar, which has implications for the chemistry occurring during carbonization.

The mass of each fatty acid in the hydrochar produced at each different HTC condition was determined and compared with its mass in the algae feedstock. Table 8 shows the fraction of each fatty acid retained in the hydrochar after HTC treatment. Most of the fatty acids in the algae, including the omega-3 and omega-7 fatty acids, were retained in the hydrochar. The total fatty acid retention was 83-86 % under all conditions, except the most severe condition examined (i.e., 220 ℃ and 30 min), where it was 67%. The reduced retention of fatty acids at this condition was primarily attributed to greater lipid losses during the transfer of reactor contents as the hydrochar produced was soft and sticky and thus impossible to collect completely from the reactor. Another reason for the low retention of fatty acids at this condition is the increased reaction of thermally unstable fatty acid components. These results and observations indicate that HTC conditions more severe than 220 ℃ and 30 min are not suitable to recover fatty acids for this species of algae.

Table 8: Effect of HTC conditions on the retention of fatty acids in hydrochar.

| Fatty | wt fraction of fatty acid retained in hydrochar after HTC | | | | | |
| | 180 °C | | 200 °C | | 220 °C | |
	15 min	30 min	15 min	30 min	15 min	30 min
C14:0	0.94	0.93	0.93	0.88	0.87	0.69
C16:0	0.91	0.93	0.94	0.94	0.93	0.78
C16:1n-7	0.94	0.96	0.97	0.95	0.96	0.79
C18:0	0.56	0.58	0.61	0.67	0.63	0.57
C18:1n-7	0.84	0.85	0.93	0.89	0.91	0.76
C18:1n-9	0.82	0.84	0.90	0.86	0.94	0.77
C18:2n-6	0.92	0.94	0.95	0.99	0.93	0.75
C18:3n-3	0.88	0.91	0.91	0.95	0.95	0.73
C20:4n-6	0.83	0.82	0.84	0.83	0.78	0.65
C20:5n-3	0.76	0.76	0.77	0.74	0.72	0.55
Total	0.84	0.85	0.86	0.85	0.83	0.67

Fatty acids containing multiple double bonds are more susceptible to isomerization, oxidation, and oligomerization during the hydrothermal treatment process. Significantly, Table 8 shows that that at least 70% of the algal EPA (i.e., C20:5n-3), a valuable polyunsaturated fatty acid, was retained even at a carbonization temperature of 220 °C, provided the carbonization time was just 15 min. To the best of our knowledge, this is the first report on the retention of EPA (i.e., C20:5n-3) in hydrochar from HTC of wet algal biomass.

Table 8 shows that only ~60% of the stearic acid (i.e., C18:0), a saturated fatty acid, was recovered from the original biomass. The recovery was nearly 100% in similar studies with a different species of algae.[56] A conclusive explanation for this difference awaits further investigation, but we suspect that the low recoveries obtained here are connected with this fatty acid being present in the original biomass in much smaller quantities than the other saturated fatty acids (see Table 7).

4.3.2. Extraction of Lipids from Hydrochar

The previous section demonstrated that HTC of this algal biomass produces hydrochar that retains ~85% of the total fatty acids in the biomass and slightly more than 75% of the valuable EPA (i.e., C20:5n-3). The remaining task, then, is to recover these lipids from the hydrochar by solvent extraction. Since some of the fatty acids have value as nutraceuticals for human consumption, we desired to use a food-grade solvent. Moreover, since algal biomass is a renewable resource, we also desired to use a solvent available from renewable resources. Ethanol meets both of these criteria, thus it was employed for the solvent extraction.

Figure 20 shows the lipid yield obtained by extracting the hydrochar produced at the different HTC conditions with ethanol. The variability in the lipid yield from the different HTC conditions is generally less than the experimental uncertainty in a given yield determination. The exception is the lipid yield at the most severe conditions, which was lower than those at the other conditions. This lower yield is very likely a reflection of lower lipid retention in the hydrochar at these more severe HTC conditions. The average lipid yield is 0.168 g per g of algae (dry basis).
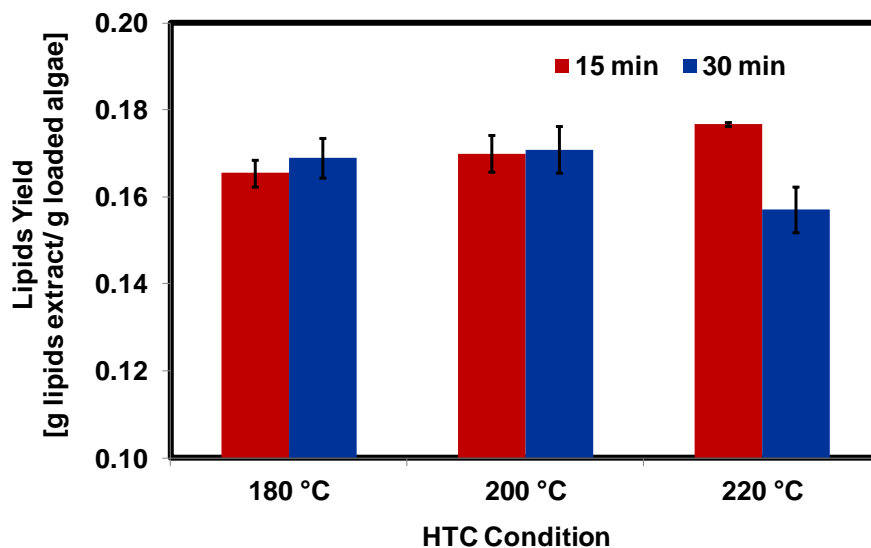
Figure 20: Effect of different HTC conditions on lipid yield. The error bars represent the standard deviation from replicate experiments.

The material extracted from the hydrochar likely contained several lipid classes such as triacylglycerides, chlorophylls, carotenoids, glycolipids, phospholipids, and sterols. The lipid components containing fatty acids are the targets for the fuel and nutraceutical products. Therefore, we quantified the fraction of the fatty acids in the hydrochar that were extracted with ethanol. We refer to this quantity as the extraction efficiency. Table 9 summarizes the results.

Table 9: Effect of HTC conditions on the extraction efficiency from hydrochar.

| Fatty | wt. fraction of fatty acids extracted from hydrochar | | | | | |
| | 180 °C | | 200 °C | | 220 °C | |
	15 min	30 min	15 min	30 min	15 min	30 min
C14:0	0.83	0.82	0.81	0.83	0.87	0.85
C16:0	0.83	0.81	0.82	0.86	0.90	0.86
C16:1n-7	0.86	0.86	0.85	0.88	0.90	0.88
C18:0	0.85	0.84	0.84	0.84	0.91	0.83
C18:1n-7	0.87	0.89	0.83	0.90	0.89	0.84
C18:1n-9	0.87	0.87	0.83	0.91	0.89	0.83
C18:2n-6	0.87	0.88	0.87	0.89	0.90	0.86
C18:3n-3	0.88	0.87	0.86	0.89	0.88	0.84
C20:4n-6	0.84	0.87	0.84	0.86	0.88	0.84
C20:5n-3	0.90	0.90	0.85	0.89	0.87	0.85
Total	0.87	0.87	0.84	0.88	0.89	0.86

The extraction protocol employed in this study provided 86 % $\pm$ 3 % recovery from the hydrochar for all of the fatty acids. Note that the fatty acids recovered from the hydrochar likely exist as both neutral lipids (e.g., monoglycerides, diglycerides, triglycerides) and polar lipids (e.g., glycolipids, glycerophospholipids). Thus, this consistent recovery of any fatty acid using a single solvent is in contrast with many previous studies, where certain solvents were only effective for extracting certain lipids with similar polarity. For instance, hexane was often used as the solvent to extract triglycerides. Moreover, the extraction efficiency showed little variation with different HTC conditions, indicating that the HTC conditions investigated in this work did not strongly affect the extraction performance. These results suggest that the milder HTC conditions may be preferable as they would consume less energy and result in less degradation of fatty acids but still provide a high lipid recovery.

Table 10: Effect of HTC conditions on the overall recovery of fatty acids from algae.

| Fatty | wt. fraction of fatty acids recovered from algae | | | | | |
| | 180 ℃ | | 200 ℃ | | 220 ℃ | |
	15 min	30 min	15 min	30 min	15 min	30 min
C14:0	0.78	0.77	0.75	0.74	0.76	0.59
C16:0	0.75	0.75	0.77	0.81	0.84	0.67
C16:1n-7	0.81	0.82	0.82	0.84	0.86	0.69
C18:0	0.48	0.49	0.51	0.56	0.57	0.47
C18:1n-7	0.72	0.75	0.78	0.79	0.81	0.64
C18:1n-9	0.70	0.73	0.75	0.78	0.84	0.64
C18:2n-6	0.80	0.82	0.82	0.87	0.84	0.65
C18:3n-3	0.78	0.78	0.79	0.84	0.82	0.61
C20:4n-6	0.69	0.71	0.71	0.72	0.69	0.55
C20:5n-3	0.69	0.68	0.65	0.66	0.63	0.47
Total	0.73	0.74	0.73	0.74	0.74	0.57

Table 10 shows the mass fraction of each fatty acid recovered from the algal biomass by this combined HTC and solvent extraction process. The results show that HTC followed by extraction can recover approximately 75% of total fatty acids, which is important for making biodiesel or green diesel fuel, and recover over 80% of the palmitoleic acid (i.e., C16:1n-7) and nearly 70% of EPA (i.e., C20:5n-3) from algae, which is important for a nutraceutical byproduct stream. To put these percentages into perspective, feeding 1 kg of the *Nannochloropsis* used in this study to a HTC-extraction process would feed 88 g of fatty acids, which includes a combined 52 g of palmitoleic acid (i.e., C16:1n-7) and EPA (i.e., C20:5n-3). The process could generate a lipid stream that contained 38 g of fatty acids for nutraceuticals and 27 g of fatty acids for biofuel production.

4.3.3. Discussion

The hydrochar generated after HTC retains ~85% of the lipids originally resident in the biomass. Importantly, about 75% of the palmitoleic acid (i.e., C16:1n-7) and EPA (i.e., C20:5n-3), which are valuable omega-7 and omega-3 fatty acids, can be recovered in this

process. These retained lipids could be readily extracted with 86% extraction efficiency using ethanol, a renewable and food-grade solvent. These observations suggest that the HTC pretreatment could be potentially applied for producing both biofuels (biodiesel or green diesel) and nutraceuticals from microalgae.

A screening of the different HTC temperatures and times indicated that HTC at 180 ℃ and 15 min produced a fatty acid recovery as high as those under the more severe conditions examined. These milder conditions would consume less energy, and hence, be preferred for HTC. The relatively brief reaction time of 15 min demonstrated here in a batch process suggests that a continuous process might be developed for the HTC processing of algae.
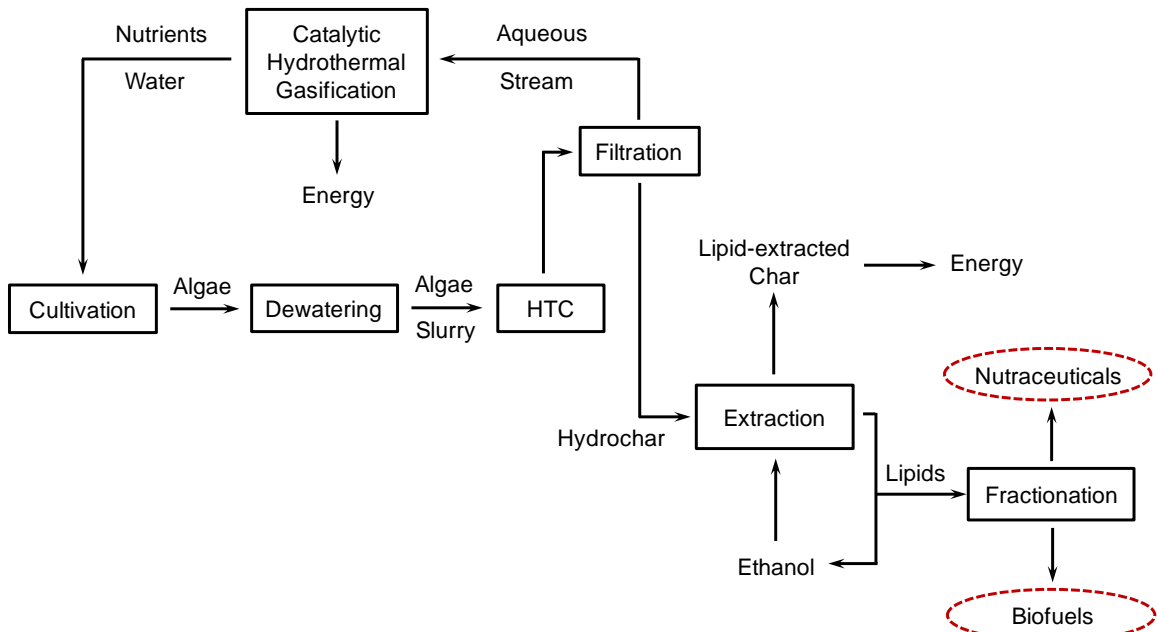
Figure 21: Conceptual process flow diagram for making nutraceuticals and biofuels from wet algal biomass via HTC

Figure 21 shows a simplified flowsheet of a possible process for using HTC to obtain nutraceuticals and biofuels from microalgae based on the results presented in the current work. The entire process uses only renewable materials. The process involves dewatering

the harvested algae to a slurry that is then treated by HTC to produce hydrochar and an aqueous stream containing nutrients along with organic compounds. Using catalytic hydrothermal gasification on this latter stream can produce fuel gases to supply heat and power in the biorefinery. The water and nutrients can then be recycled to the algae pond. Previous studies have demonstrated that this aqueous phase co-product could support algal growth and potentially reduce the amount of synthetic fertilizers required by the algal biorefinery.[58] The hydrochar is extracted with ethanol to recover the lipids, which can then be further fractionated to isolate nutraceuticals and biofuel precursors. The ethanol is recovered and recycled. In addition to the fuel and nutraceutical products, the process generates lipid-extracted hydrochar that could be gasified or directly burned to provide thermal energy, or potentially be provided as animal feed. In summary, the results presented in this work demonstrated that the HTC-ethanol extraction procedure may offer an improvement over the more traditional wet hexane extraction process or the supercritical CO_2 extraction approach.

4.4 Conclusions

HTC of microalgae produced hydrochar, and the char yield is a linear function of the log of the reaction ordinate, which measures the severity of the hydrothermal treatment conditions. The HTC of 15 wt.% *Nannochloropsis* sp. slurry at 180-200 ℃ and 15-30 min produced a solid hydrochar that retained more than 85% of the total fatty acids, about 95% of the palmitoleic acid (i.e., C16:1n-7) and 75% of the EPA (i.e., C20:5n-3) in the original biomass. Approximately 86% of retained fatty acids could be extracted using ethanol, thereby resulting in a total recovery of 74%. These results suggest that HTC

followed by ethanol extraction is a promising method to produce algal lipids that have value for both biofuels and nutraceuticals.

CHAPTER 5

Supercritical Water Gasification of Lipid-extracted Hydrochar to Recover Energy and Nutrients

5.1 Introduction

Microalgae are receiving increasing attention as a renewable feedstock for making biofuels and nutraceuticals as they grow quickly, have low land requirement compared to terrestrial biomass, and can be cultivated to contain diverse lipid contents and compositions.[44] One technical challenge in the process of producing algal oil is to extract efficiently and economically the lipids of interest from algal cells. Extractions with organic solvents and with supercritical CO_2 are the two lipid-extraction techniques that have been investigated the most.[49] Both of these techniques work best when the algal biomass has low moisture content, as excess water can hinder the effective contact between biomass and extraction solvents, leading to poorer extraction performance.[54] Algal biomass, however, naturally contains water and therefore usually needs to be dried prior to an extraction step. This drying step consumes a significant amount of energy that cannot easily be recovered because of the low temperature at which it would be available. Such energy inputs need to be avoided or minimized.[45]

To obviate the energy-intensive drying step, several studies used hydrothermal carbonization (HTC) to facilitate the subsequent extraction of algal lipids.[61-62,69] HTC is a process that subjects a wet algal slurry to elevated temperatures (~200 ℃) and pressures above the saturation pressure of water at the HTC temperature. The main products after HTC are solid particles, also known as hydrochar, and an aqueous phase containing numerous components including potential algae nutrients (N-containing compounds) and organic compounds. The hydrochar is easy to separate from the aqueous phase by simple filtration, and it retains a large proportion of the lipids in the original biomass.[61-62] The retained lipids can be readily recovered by extraction using organic solvents.[61-62,69] The aqueous phase co-product has been shown to support algal growth and its recycling could potentially reduce the capital costs required for the algae cultivation.[58] Due to these advantages, the HTC-Extraction approach is potentially a simple and efficient method for biodiesel production.[61-62] In addition, we recently demonstrated that eicosapentaenoic acid (EPA), a valuable omega-3 fatty acid having health benefits, can be recovered from wet algae via this approach using only water and ethanol, a non-petroleum-derived solvent.[69] Thus, the HTC-Extraction approach offers a path to making nutraceuticals as a high-value byproduct from microalgae.

The post-extraction hydrochar, which we refer to as lipid-extracted hydrochar (LEH), primarily consists of carbonized polysaccharides and proteins.[60] This material could conceivably be used as a soil amendment, as a raw material for producing various carbons, or even as a feed supplement for livestock. These uses would divert the material away from the biorefinery, however, and prevent recovery of the chemical energy and nitrogen in the LEH. Previous studies showed that hydrochar typically has a mass

fraction of nitrogen similar to that of the starting algal biomass.[57-58] Given that the extracted lipids contain very little nitrogen, it is likely that the majority of the nitrogen in the hydrochar will be retained in the LEH after lipid extraction. Nitrogen is an essential nutrient in algal cultivation. Consequently, the chemical energy and nitrogen contained in the LEH, if recovered and recycled, could improve the economics and sustainability of a HTC-extraction biorefinery.

In the present work, we seek to gasify the LEH in supercritical water (T_c=374 ℃, P_c=22.1 MPa) for energy recovery and nitrogen recycling. Ideally, supercritical water gasification (SCWG) would produce fuel gases (i.e., CH_4 and H_2) that can provide thermal energy and electricity in a biorefinery along with partitioning the N in the hydrochar to the aqueous phase where it can be recycled to promote additional algal growth. Of the different gasification options that exist, SCWG is unique in providing the possibility of recovering nitrogen in a bioavailable form during the simultaneous production of fuel gases. Various types of biomass, including cellulose,[70] lignin,[70] microalgae,[71] and macroalgae,[72] have been successfully gasified to fuel gases in SCW with low yields of tar and char.[73] In addition to producing high quality syngas, Cherad *et al.* demonstrated that the process water from SCWG of macroalgae contains ammonium and can support algae growth.[72] These previous studies suggest SCWG is a promising technique to convert the residual LEH to fuel gases and recycle nutrients. We herein report on experiments wherein LEH was gasified in supercritical water at various temperatures and times. We have determined the effects of process variables (i.e., temperature and time) on the gas yield and the recovery efficiency of nitrogen from LEH. To the best of our knowledge, this study is the first report on SCWG of LEH, and we

demonstrate the suitability of this approach for energy recovery and nitrogen recycling. We note that Castello *et al.* recently reported on SCWG of a hydrochar from lignocellulosic biomass,[74] but that material had a much lower nitrogen content than LEH. We focus on uncatalyzed SCWG because solid gasification catalysts are not likely to be effective in promoting the gasification of the solid LEH particles.

5.2 Material and Methods

This section provides information about the algae and reactors used in this work and the procedures employed for HTC, lipid extraction, and SCWG. It concludes with a discussion of the methods used to analyze the gaseous and aqueous-phase products from SCWG.

5.2.1. Materials

The algal biomass used in this work was a 21 wt.% slurry of *Nannochloropsis sp.* provided by Valicor Renewables. The algae contained 8.8% fatty acids (measured as fatty acid methyl esters) in total on a dry weight basis, and polyunsaturated fatty acids accounted for more than 50% of the total mass of fatty acids. The complete fatty acid profile has been reported in our previous study.[69]

All HTC and SCWG experiments were conducted in mini-batch reactors. The reactors have approximately 4.1 ml internal volume and were assembled from 316 stainless steel Swagelok parts (2 caps and 1 port connector). When used in SCWG experiments, the cap on one end of the reactor was replaced by a reducing union, which was fitted with a 9 in. length of 0.125 in. o.d. tubing with a wall thickness of 0.035 in. This tubing was connected to a high-pressure valve (HiP part 15-12AF2). All assembled reactors were first loaded with water and treated at 500 °C for 1 h to remove any residual organic

71

impurities inside the reactor chamber and to season the reactor walls prior to conducting SCWG experiments. The reactors were then thoroughly washed with acetone and water, and air-dried.

All chemicals used in this work (i.e., anhydrous ethanol, methanol, acetyl chloride, and tricosanoic methyl ester) were analytical grade and obtained commercially. Helium, hydrogen, and argon were obtained from Cryogenic Gases. Analytical gas standards were purchased from Air Liquide Specialty Gases.

5.2.2. HTC and Lipid Extraction Procedure

The LEH used for SCWG experiments was generated by HTC of a wet microalgal slurry followed by ethanol extraction. The experimental details appear in Chapter 4,[69] so we give only a brief overview here. Approximately 3 g of the homogenized 15 wt.% microalgal slurry was loaded into each reactor. The HTC experiment was conducted by immersing sealed reactors in a preheated, isothermal fluidized sand bath at 180 °C for 15 min and then quickly removing them and cooling them in room-temperature water. We selected this mild carbonization condition as previous work showed that it provides a fatty acid recovery as high as those at the higher carbonization temperatures examined.[69] The produced hydrochar was thoroughly washed with water, completely dried, and subjected to a two-stage batch-wise extraction with anhydrous ethanol at 60 °C. This extraction procedure has been shown to recover approximately 90% of the fatty-acid-containing lipids from the hydrochar.[69] After extraction, the LEH was dried in an oven overnight to evaporate any residual ethanol. Portions of the algae, hydrochar, and LEH were reserved for elemental analysis by Atlantic Microlab, Inc.

5.2.3. SCWG Procedure

In a typical SCWG experiment, 0.0232g of LEH and 0.445g of deionized water were loaded into a reactor, providing a water density of 0.1 g/cm^3 at supercritical conditions and a solid loading of 5.0 wt%. This water loading provided sufficiently high water pressure to maintain a single supercritical phase during reactions. The residual air inside the reactor was removed by evacuating and charging the reactor with helium for several times. After the last evacuation, 50 psi of helium was charged into the reactor, and it served as an internal standard during the gas analysis. The loaded and pressurized reactor was then placed in a preheated, isothermal, fluidized sand bath for the desired amount of time to provide the thermal energy needed to drive the gasification reactions. After the desired reaction time had elapsed, the reactor was removed from the sand bath and cooled to room temperature by a fan. Prior to analysis, the reactor was held at ambient conditions for at least 1 hr to allow the liquid-gas system to reach equilibrium and for the gas phase composition to become uniform. We examined SCWG temperatures between 450 and 600 ℃ and reaction times from 10 to 360 min. Water density (0.1 g/cm^3) and solid loading (15 wt.%) were the same at all conditions as these variables tend to have less impact on SCWG results than do temperature and time.[71] All SCWG experiments were replicated and along with the mean values, standard deviations are reported as a measure of the experimental uncertainties.

5.2.4. Gas-phase Analysis

The gas phase was analyzed with an Agilent Technologies model 6890N gas chromatograph (GC) equipped with a thermal conductivity detector (TCD). Each gas component in the mixture was separated by a 15 ft × 1/8 in. i.d. stainless steel column,

packed with 60 × 80 mesh Carboxen 1000 (Supelco). Argon at a constant flow rate of 15.0 mL/min served as the carrier gas for the analysis. The oven temperature was initially held at 35 ℃. After a 2 min hold, the temperature was ramped at 10 ℃/min to 225 ℃. The final temperature was held for 10 min.

The mole fraction of each gas product was determined from its peak area by using calibration curves that were generated from the analysis of commercial analytical gas standards with known composition. The molar amount of each gas constituent was then calculated from the known composition and the known amount of helium (i.e., 50 psi) added to the reactor prior to SCWG reaction. The yield of each gas species was expressed as its molar amount divided by the mass of LEH loaded into the reactor.

5.2.5. Aqueous-phase Analysis

After analyzing the gas fraction, we opened the reactors and transferred the aqueous phase to a 15 ml centrifuge tube. The reactor was then thoroughly washed twice with 5 ml aliquots of water to ensure that all water soluble contents were collected. All the liquid collected was then combined and centrifuged (4000 RCF × 5 min) to remove any solid particles that might be present. After centrifugation, the top liquid phase was collected and stored at 4 ℃ prior to analysis.

We measured the concentration of total-N and NH_3-N in the aqueous phase with a HACH Total Nitrogen Reagent Set and HACH nitrogen-ammonia reagent set, respectively. Prior to analysis, the aqueous phase was further diluted (1:8) with deionized water to a concentration within the kit measurement range. A Thermo Scientific Genesys 20 spectrophotometer was used to measure the absorbance of analyte solutions. The

concentration of analyte was determined by using linear calibration curves generated from standard solutions with known concentrations.

5.3 Results

This section starts with the report of the elemental composition of algae, hydrochar, and LEH. It then provides the results regarding the influence of temperature and time on the gas yields as well as the recovery of nitrogen in the aqueous phase from SCWG of LEH. The section concludes with a discussion of the results, their significance to the field, and a conceptual process flow diagram showing how the findings can be integrated into the previously developed procedure of recovering algae oil using the HTC-extraction approach.

5.3.1. Elemental Composition of Algae, hydrochar, and LEH

Table 11 Elemental composition of materials and yields of hydrochar and LEH (wt%, dry basis)

	C	H	N	S	Yield
Algae	46.81	6.64	7.26	---	---
Hydrochar	57.23	7.94	5.97	---	45
LEH	50.06	6.62	8.8	0.63	62

Note: The yield of hyodrchar is its mass divided by the mass of dry algae loaded into the reactor. The yield of LEH is its mass divided by the mass of hydrochar loaded into the reactor.

Table 11 gives the elemental composition of the algae, hydrochar, and LEH along with the mass yields of each product. We calculate these gravimetric yields as the mass of product recovered (i.e., hydrochar, LEH) divided by the mass of the starting material (i.e., algae, hydrochar). The hydrochar is enriched in C and H relative to the initial algal biomass. It retained 55% and 37%, respectively, of the C and N in the original microalgae. These results are similar to those reported previously for similar microalgae carbonization experiments.[58] The LEH that remained after lipid extraction from the

hydrochar was a powdery solid with dark brown color. A comparison of the elemental compositions and masses of hydrochar and LEH revealed that the extraction process removed approximately 45% of the carbon but only 8% of the nitrogen from the hydrochar. The relatively low removal of nitrogen is expected as the lipids being extracted contain little nitrogen. The LEH contained about 30% and 34% of the C and N, respectively, in the original microalgae. Being able to recover the chemical energy in the C and the nutrient value in the N would enhance the sustainability of a biorefinery that employed HTC-extraction. Therefore, the LEH was used as the feedstock for the SCWG experiments.

5.3.2. SCWG at 450 ℃
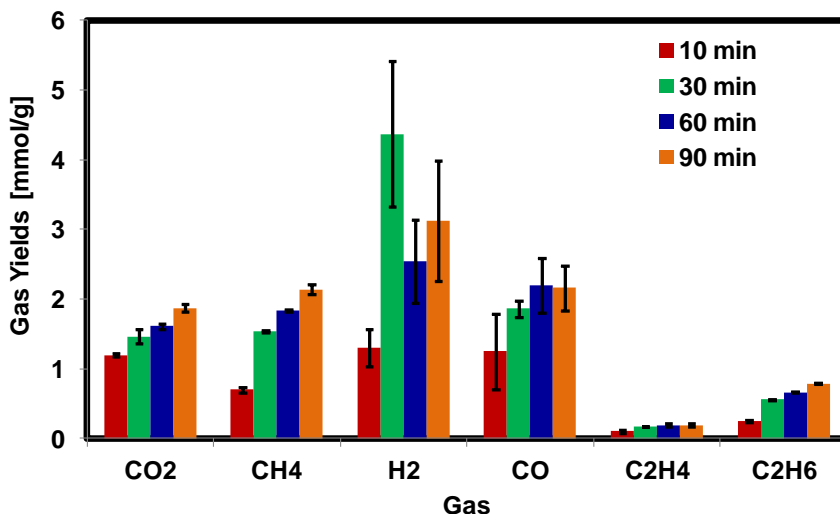
Figure 22: SCWG of LEH at 450 ℃ (0.1 g/cm^3 water density, and 5.0 wt % solid loading). The error bars represent the standard deviation from replicate experiments.

Figure 22 shows the temporal variation of the yields of the gaseous products from SCWG of LEH at 450 ℃ with a water density of 0.1 g/cm^3 and a solid loading of 5.0 wt%. The gas products were CO_2, CH_4, H_2, CO, C_2H_4, and C_2H_6. With just a few exceptions, the yields of CO_2, CH_4, H_2, and CO were comparable to one another at any given batch holding time investigated, whereas C_2H_4 and C_2H_6 were present in yields

lower than the other gas products. The yields of CO_2 and CH_4 increased with time. The yield of CO initially increased with time and then reached a level value. The yield of H_2 showed a large increase between 10 and 30 min. This increase in H_2 yield during the first 30 min was probably due to the fast steam reforming reactions.[75-76] A portion of the H_2 produced was then converted to methane via methanation as time progresses, which was reflected by the decreasing H_2 yield and the increasing CH_4 yield at longer reaction time. Interestingly, considerable amounts of CO were present at all batch holding time studied at this temperature. This outcome differs from some previous SCWG studies in metal reactors where CO yields were lower.[71] This higher yield of CO in this study indicates that the CO-forming reactions (e.g., steam reforming, decomposition) dominated over CO-consuming reactions (e.g., water gas shift) at this temperature.

5.3.3. Effect of Temperature
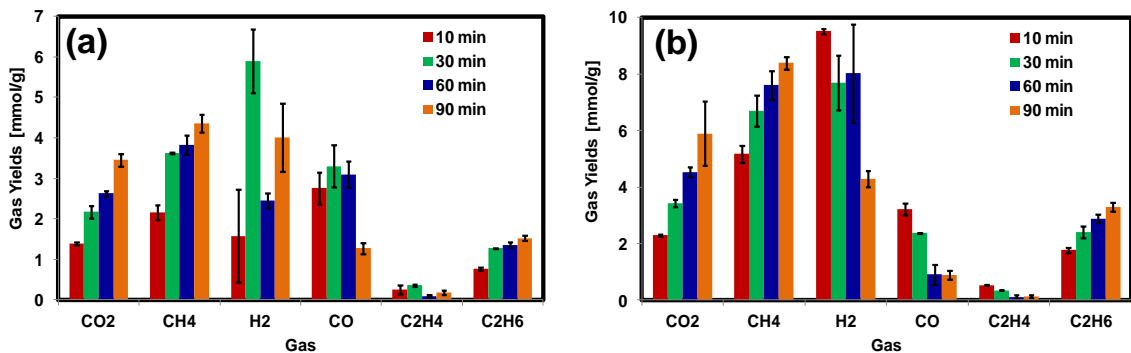
Figure 23: Effect of batch holding time on yields of gaseous products (0.1 g/cm^3 water density and 5.0 wt % solid loading) at (a) 500 ℃ and (b) 550 ℃. The error bars represent the standard deviation from replicate experiments.

Figure 23 shows the temporal variation of the yields of the gaseous products from SCWG of LEH at 500 ℃ and 550 ℃ with a water density of 0.1 g/cm^3 and a solid loading of 5.0 wt%. For CO_2, CH_4, H_2, and C_2H_6, at a given batch holding time the higher reaction temperature provided the higher gas yield. CO was an exception, as the higher temperatures produced lower yields, presumably because of faster rates of the water gas

77

shift reaction. The yields of each gas species at 500 ℃ displayed trends with time very similar to those observed at 450 ℃. At 550 ℃, however, the yields of H_2 and CO decreased at longer reaction time. These trends suggest the conversion of CO and H_2 to CH_4 and CO_2 *via* the water-gas shift and methanation reactions at longer batch holding time.

We used the gas yields at 10 min at each temperature to estimate the activation energy (E_a) for the initial formation rate of each gas product. A similar approach has been used in previous studies to elucidate the formation paths for the different gaseous products.[70-71] The apparent activation energies determined by this approach were 32 ± 1 kJ/mol for CO_2, 99 ± 1 kJ/mol for CH_4, 97 ± 12 kJ/mol for H_2, 47 ± 28 kJ/mol for CO, 79 ± 11 kJ/mol for C_2H_4, and 97 ± 1 kJ/mol for C_2H_6. The average activation energy for H_2 formation (97 kJ/mol) is three times that for CO_2 formation (32 kJ/mol), indicating that these two gas products do not form exclusively in the same reaction path (e.g., steam reforming). In addition, the activation energy for H_2 formation from LEH (97 kJ/mol) is indistinguishable from E_a of ~100 kJ/mol for H_2 formation from SCWG of microalgae.[71] Likewise, for both algae and LEH, E_a for CO_2 formation from SCWG was much lower than E_a for formation of either CH_4 or H_2. These similarities suggest that LEH and microalgal biomass may be undergoing some similar reactions during SCWG and that LEH is no more difficult to gasify than algal biomass.

Figure 24: (a) Carbon yield and (b) energy recovery at different temperatures and batch holding times (0.1 g/cm³, 5.0 wt% loading). The error bars represent the standard deviation from replicate experiments.

Figure 24(a) reports the carbon yield at each temperature and batch holding time. This quantity, sometimes referred to as the carbon gasification efficiency, is the percentage of the carbon loaded into the reactor that is converted into gaseous products. As expected, the carbon yield increases with both temperature and batch holding time. At all temperatures investigated, the carbon yield initially increased quickly followed by a much more gradual increase or even plateau region after 30 min. These results indicate that some portion of the LEH is relatively easy to gasify at these temperatures whereas other portions are much more recalcitrant. This outcome is consistent with a previous study on SCWG of algae where "fast" and "slow" gasification paths were postulated.[71]

As the main purpose of producing fuel gases from LEH is to provide thermal energy for an algal biorefinery, we calculated the energy recovery at each SCWG condition. This quantity is the higher heating value of the gas products (i.e., CH_4, H_2, CO, C_2H_4, and C_2H_6) relative to the heating value of the LEH, which we estimated by the Dulong formula, defined as Equation (21).[77]

$$\text{Heating Value } (\text{MJ/kg}) = 0.338C + 1.428(H - O/8) + 0.095S \qquad (22)$$

C, H, O, and S are the weight percentages (%) of carbon, hydrogen, oxygen, and sulfur in the LEH, respectively, as measured by Atlantic Microlab, Inc. The energy recovery is

79

the percentage of the chemical energy in LEH that is transferred to the gaseous products. Figure 24(b) shows the results. The trends of energy recovery with batch holding time and temperature are similar to those for the carbon yield. While the gas products at 450 ℃ contain only 23.8 ± 2.1 % of the chemical energy of the initial LEH, the energy recovery reaches 39.3 ± 1.9 % at 500 ℃ and 68.2 ± 1.3 % at 550 ℃. These energy recoveries are similar to those obtained for SCWG of algal biomass at comparable conditions.[71] It is presumable that even higher energy recoveries can be achieved at more severe gasification conditions and we provide evidence to this end in a subsequent section.

5.3.4. Analysis of Total-N and Ammonia-N in the Aqueous Phase

The aqueous phase generated from the SCWG of LEH emitted a foul odor and was light yellow in color. The color was likely caused by the gasification products of amino acids.[78] As discussed in Section 5.3.1, the LEH retained approximately 30% of the nitrogen in the starting microalgae. To evaluate the performance of SCWG in recovering this nitrogen from LEH, we quantified the concentration of total-N in the aqueous phase. To facilitate a meaningful evaluation, we define the total-N recovery as the mass fraction of nitrogen loaded into the SCWG reactor that was recovered in the aqueous phase. Figure 25(a) shows that the total-N recovery was around 100% for all SCWG conditions tested. Thus, the complete recovery of nitrogen in the aqueous phase was achieved at all the SCWG conditions investigated in this work. Since the run-to-run variability in the total-N recovery is generally less than the experimental uncertainty, no statistical trend with respect to the SCWG temperatures and times can be discerned.
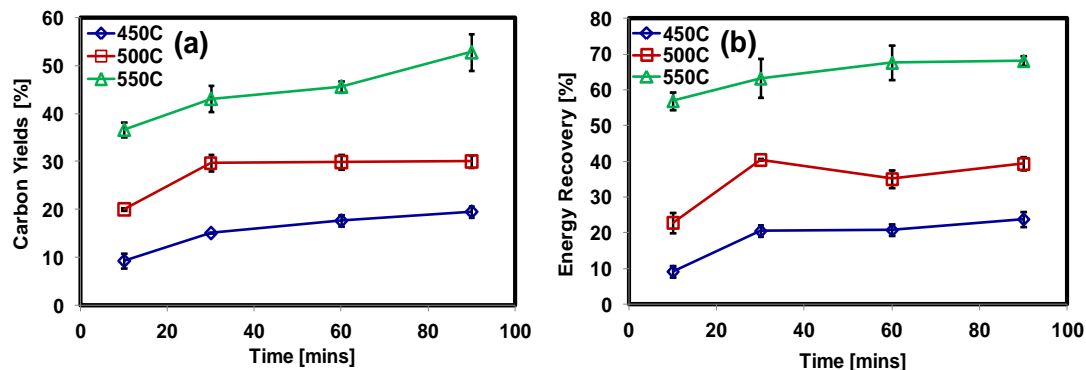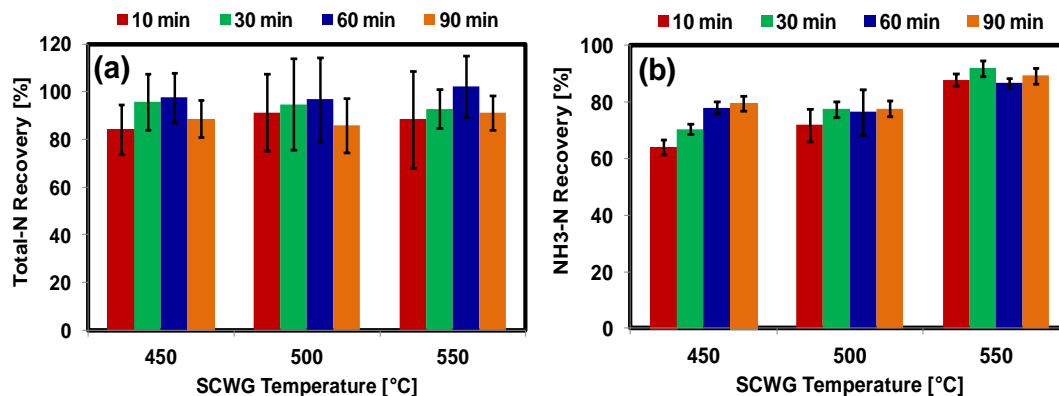
Figure 25: (a) Total-N Recovery and (b) NH$_3$-N Recovery at different temperatures and batch holding times (0.1 g/cm^3, 5.0 wt% loading). The error bars represent the standard deviation from replicate experiments.

As ammonium has been widely used as a nitrogen source in algae cultivation, we further quantified the concentration of NH$_3$-N in the aqueous phase. Ammonium likely forms from organic nitrogen by hydrolysis and elimination reactions involving water molecules. We define the NH$_3$-N recovery as the mass fraction of nitrogen loaded into the SCWG reactor that was recovered in the aqueous phase in NH$_3$ form. These results appear in Figure 25(b). The NH$_3$-N recovery generally increased with increasing reaction severity. It was 64% at the mildest condition studied (i.e. 450 ℃ and 10 min), and increased to almost 90% at 550 ℃ and 90 min. These results suggest that at more severe SCWG conditions, more of the aqueous-phase N-containing compounds were converted to ammonium.

5.3.5. SCWG at 600 ℃

The previous section provided a systematic study of the influence of temperature and time on SCWG of the LEH. Those results suggest that higher temperature and longer batch holding time favor both the recovery of energy and nitrogen from LEH *via* SCWG. An energy recovery of 75% and approximately 90% nitrogen recovery as ammonium

were achieved after SCWG at 550 ℃ and 90 min. To improve further the recovery efficiency, we conducted SCWG at a final more severe condition of 600 ℃ and 6 hr.
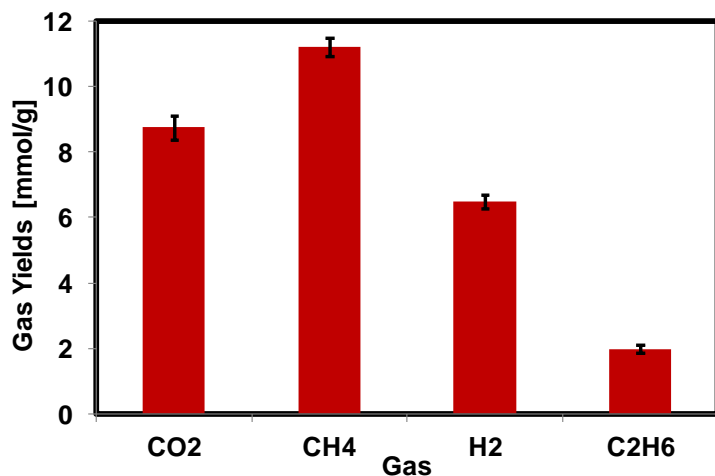
Figure 26: SCWG of LEH at 600 ℃ for 6 hrs (0.1 g/cm^3 water density, and 5.0 wt % solid loading). The error bars represent the standard deviation from replicate experiments.

Figure 26 shows the gas yields from SCWG of LEH at 600 ℃ for 6 h. CH_4 was the major gas product, followed by CO_2 and H_2, respectively. The yields of these three main gas products were about 50% higher than those obtained from SCWG at 550 ℃ and 90 min. A considerable amount of C_2H_6 was also detected, but in yields lower than those of the other gas species. Though CO and C_2H_4 were present in the gas products of SCWG at 450-550 ℃, neither product was detected from SCWG at 600 ℃. As noted earlier, the accelerated rate of water gas shift and methanation can account for the disappearance of CO, and hydrogenation to ethane can account for the absence of ethylene. The large amounts of CH_4 and CO_2 in the gas products also suggest that water-gas shift and methanation are the two reactions that likely dominate under this condition. A carbon yield of 57.4 ± 1.9 % and energy recovery of 72.3 ± 2.0 % were achieved at 600 ℃ for 6 h. This energy recovery is just slightly higher than that achieved at 550 ℃ and 90 min, which is 68.2 ± 1.3 %. Though the higher yields of CH_4 and H_2 at 600 ℃ for 6 h make a

positive contribution to the energy recovery, part of this gain is offset by the absence of CO and C_2H_4 in the gas products. It should be noted that even if relatively long reaction time has been applied, it is likely that the thermodynamic equilibrium under 600 ℃ has not been achieved yet due to kinetic limitation.[74,76] In theory, running the gasification reaction longer could improve the carbon and energy recovery. Unfortunately, we were not able to provide such results as we found that performing the reactions longer at 600 ℃ caused significant gas leaks. Another option to achieve more complete gasification is to use proper catalysts, as demonstrated by previous study where complete gasification of the microalgae was achieved with a Ru/C catalyst loading of 2 g/g.[79] However, no previous work has studied the effectiveness of catalysts in SCWG of LEH and this topic requires further investigation. To summarize, it appears that a carbon yield of 55-60% and an energy recovery of 70-75% are the upper bounds of what can be achieved by noncatalytic SCWG of this LEH at 600 ℃ or below in this work.

The aqueous phase generated at this condition was colorless, suggesting a more complete gasification of N-containing compounds than was observed at the lower temperatures. An analysis of the aqueous phase showed a total-N recovery of 94.0 ± 12.4 % and NH_3-N recovery of 97.2 ± 2.3 %. These results are significant as they show that SCWG at 600 ℃ and 6 hr could completely recover N from LEH in the process water as ammonium.

5.4 Discussion

The previous section showed that the LEH generated from the HTC-extraction procedure was successfully gasified in SCW with the nitrogen recovered in the aqueous phase as ammonium. An energy recovery of nearly 75% and complete nitrogen recovery

as ammonium were achieved after SCWG at 600 ℃ and 6 h. Though these conditions are severe, a well-engineered process would be designed to recover the thermal energy in the SCWG effluent stream.
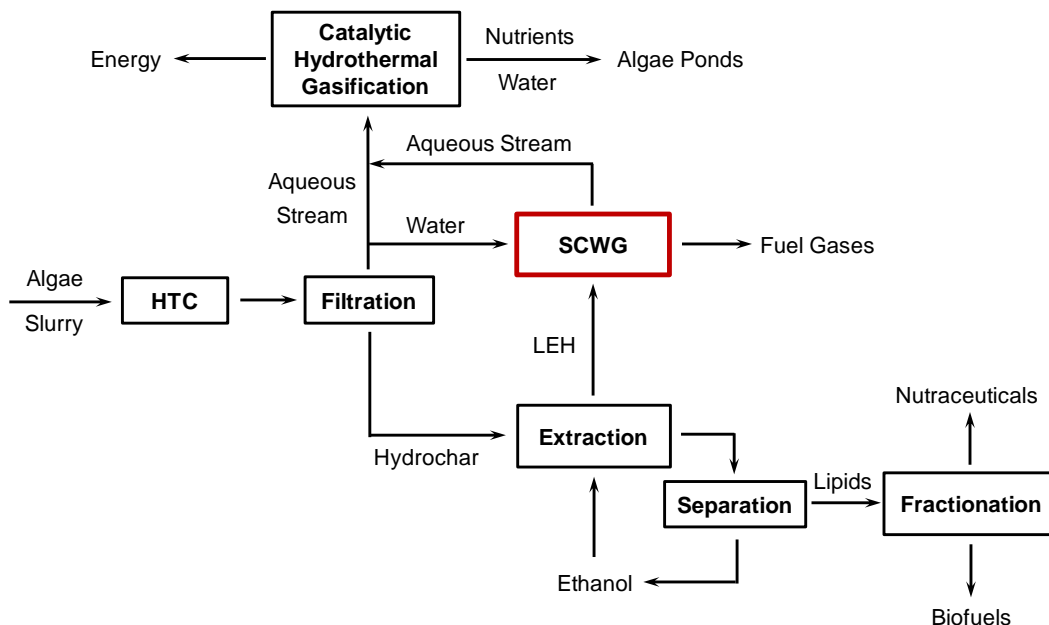
Figure 27: Expanded process flow diagram for recovering oil from wet algal biomass

We previously proposed a conceptual process flow diagram for making nutraceuticals and biofuels from wet algal biomass *via* a HTC-Extraction approach.[69] Briefly, an algae slurry undergoes HTC to produce hydrochar along with an aqueous stream that can be recycled. Contacting the hydrochar with warm ethanol extracts the lipids, which can then be fractionated into high-value omega-3 fatty acids for nutraceuticals production and other fatty acids for biofuels production. Figure 27 illustrates the steps and extends this previous work by demonstrating how the results presented in the current work can be integrated into the process. SCWG of the LEH produced in the extraction step produces fuel gases and an aqueous stream that still contains some carbon and is rich in ammonium. The latter stream can be combined with the aqueous stream generated after HTC. Performing catalytic hydrothermal gasification on this combined stream can produce

additional fuel gases to supply heat and power in the biorefinery. The water and nutrients can then be recycled to the algae pond. Additionally, the H_2 produced by SCWG of the LEH, if separated from the gaseous product, could also be used for the hydrogenation of unsaturated lipids extracted from the algae for biodiesel production. In summary, the results presented in this work suggest that the SCWG of LEH may be of utility in the process of isolating nutraceuticals and making biofuels from microalgae.

5.5 Conclusions

SCWG of LEH produced gaseous products containing H_2, CO_2, CH_4, CO, C_2H_4, and C_2H_6, and an aqueous phase containing nitrogen recovered from the LEH as ammonium. Increased reaction temperature and time enhanced the energy and nitrogen recoveries. An energy recovery of 75% and complete nitrogen recovery as ammonium were achieved after SCWG at 600 ℃ and 6 hrs. The activation energies for forming carbon oxides were <50 kJ/mol whereas activation energies for formation of H_2 and saturated hydrocarbons were ~100 kJ/mol. The results demonstrate that SCWG can convert the LEH to materials that promote the sustainability of an algal biorefinery that employs carbonization and lipid extraction to make biofuels and high-value nutraceuticals.

CHAPTER 6

Summary, Conclusions and Future Work

6.1 Summary and conclusions

The first half of this dissertation clarified important aspects of wax deposition behaviors when operation conditions (i.e., temperature and flow rate) vary, which were previously overlooked or misinterpreted. Despite the fact that many previous studies have used the "thermal driving force" to characterize the effect of temperature on wax deposition, it was not the most comprehensive predictive parameter, as it neglects the importance of the solubility curve on wax deposition. We revealed that the most important factors affecting deposition behavior when the oil and coolant temperatures are changed are the mass driving force and the shape of the solubility curve. To capture the impact of the solubility curve on wax deposition, we developed a characteristic mass flux for wax deposition, $J_{wax,c}$, which includes the diffusivity, $D_{wo,wall}$, and the mass driving force, $[C_{oil}(eq) - C_{wall}(eq)]$.This criterion was applied to analyze two sets of deposition experiments using either a model oil system or a crude oil system, and the theoretical analysis was consistent with the experimental observation. These findings showed that the mass driving force, $[C_{oil}(eq) - C_{wall}(eq)]$, is a more appropriate parameter to predict the temperature effects on wax deposition in comparison to the thermal driving force $[T_{oil} - T_{coolant}]$.

Next, we analyzed the experimental trend of reduced deposit thickness with increasing flow rate. Three effects were found to affect deposition behavior when the oil flow rate is changed. These effects include the influence of the boundary layer thickness (Effect 1), the diffusivity at the interface (Effect 2), and the interface wax concentration (Effect 3) on heat and mass transfer. The first two effects tend to increase the deposit growth rate while the third one decreases it, and the overall effect is dependent on the competition among them. More importantly, this study revealed that the dynamics of the competition among these three effects can vary as time progresses and that Effect 3 eventually dominates the other two effects. The time-variation trends of these three effects are consistent with the experimental observation. Therefore, we herein provided an alternative explanation to the experimental trend from first principles, as opposed to the reason of "shear removal" used in previous work.

Another piece of the dissertation is focused on developing methods to promote the sustainable production of biofuels and nutraceuticals from microalgae. Microalgae hold great promise for renewable fuels and chemicals, but to date it is still difficult to commercialize this route due to the high cost and technology challenges associated with producing algal oil.[7] We first proved that hydrothermal carbonization (HTC) of algal biomass followed by warm ethanol extraction can extract algal lipids that have values for both biofuels and nutraceuticals. The HTC of 15 wt.% *Nannochloropsis* sp. slurry at 180-200 °C and 15-30 min produced a solid hydrochar that retained ~85% of the total fatty acids, ~95% of the palmitoleic acid, and ~75% of the EPA in the original biomass. Approximately 86% of retained fatty acids could be extracted using ethanol, thereby resulting in a total recovery of 74%. Thus, we herein demonstrated for the first time a

process for removing fatty-acid-containing lipids from wet algae using only water and a non-petroleum-derived solvent. This is also the first work showing that the HTC-extraction approach can recover the high-value omega-3 fatty acids (e.g., EPA) from wet algae. These observations suggest that the HTC pretreatment could be potentially applied for producing both biofuels (biodiesel or green diesel) and nutraceuticals from microalgae.

We then showed that supercritical water gasification (SCWG) of the lipid-extracted algal hydrochar (LEH) at 450-600 ℃ produced H_2, CO_2, CH_4, CO, C_2H_4, and C_2H_6, and converted the organic-bound nitrogen in the LEH into ammonium in the aqueous phase. Increased gasification severity increases the energy and nitrogen recovery. An energy recovery of 75% and complete nitrogen recovery as ammonium were achieved after SCWG at 600 ℃ and 6 hrs. These findings demonstrated for the first time the conversion of the byproduct LEH to materials that can be used within an algal biorefinery. Recovering energy and nutrients in this manner may promote the sustainability of an algal biorefinery that employs carbonization and lipid extraction to make biofuels and high-value nutraceuticals.

6.2 Future Wax Deposition Studies

Wax deposition is a crucial operational challenge to the oil and gas industry. Despite several decades' research efforts, today the application of wax modeling for field design still faces significant challenges. Several aspects of the fundamental deposition physics are not fully understood yet. For instance, it was noted by many experimental studies that part of the formed deposit could be removed by the moving fluid, especially in the flow regime with relatively high Reynolds numbers. However, the fundamental physics of this

"shear removal" effect is not understood, nor is the mathematical description available. Failure to correctly incorporate this effect into the deposition model might lead to inaccurate prediction for cases with high oil flow rates. Plus, the fluids transported in field pipelines are usually multiphase flow, such as oil-gas flows, oil-water flows, or sometimes oil-gas-water three phase flows. But very few experimental studies have attempted to understand the effects of the interplay between phases on wax deposition from fundamental perspectives of view. Lack of these experimental characterizations inhibits the development of fundamental wax deposition models for multiphase flows. Most of the developed multi-phase deposition models are still highly-empirical and are insufficient to provide accurate predictions for the field. It would be essential to take further research and development efforts to understand the wax deposition fundamentals and improve the efficiency of the deposition models in multiphase flows.

6.3 Outlook for Algae Studies

Microalgae hold great promise for nutraceuticals and biofuels. In this dissertation we developed several processes that have potential to promote the recovery of algal oils. The emphasis herein is on proof-of-concept. Further investigations should focus on the influence of multiple process variables on the product yield and quality. Plus, a more fundamental mechanistic understanding of the underlying chemistry of HTC and SCWG process is necessary if detailed kinetic models are to be developed for process optimization. Several other technological issues must be considered as well during commercialization, such as feedstock transport, solids handling, and energy recovery, as well as designing large-scale reactors that can maintain high pressures and temperatures. Conducting life-cycle assessment and techno-economic analysis of the conceptual

process designs would be beneficial to assess the economics and sustainability of these pathways for algal oil production.[80] Finally, research efforts in the other phases of algal biorefinery would also be essential, including screening algae species that have desirable lipid content and composition, as well as developing efficient and economically viable approaches to purify and fractionate the extracted lipid crudes. We included several reviews of these topics for those who might be interested.[11,45-47]

Appendix A

Calculations of the Characteristic Mass Flux for Wax Deposition at $\delta > 0$

The calculations of the parameters for the characteristic mass flux, $J_{wax,c}$, at t $= 0$ ($\delta = 0$) are previously shown in Table 1 (for experiments with different T_{oil}) and Table 2 (for experiments with different $T_{coolant}$). To validate that the $J_{wax,c}$ follows the same trend with respect to the changes in T_{oil} and $T_{coolant}$ for a given thickness of the deposit, Table A.1 and Table A.2 list the parameters of $J_{wax,c}$ at $\delta > 0$.

Table A.1 Comparison of the parameters for the characteristics mass flux for wax deposition, $J_{wax,c}$, among the deposition experiments when $\delta = 0.34$ mm with different T_{oil}, while Q_{oil} and $T_{coolant}$ are maintained constant.

Parameters	Value			
Experimental Operating Conditions				
T_{oil}, ^{0}C	15.3	20.3	25.3	35.4
$T_{coolant}$, ^{0}C	5.0			
Q_{oil}, m^3/h	20.0			
Model Calculations				
t, h	1.32	1.94	2.55	10.35
T_{wall}, ^{0}C	12.98	17.10	21.23	29.74
$D_{wo,wall} \times 10^{10}$, m^2/s	2.55	3.14	3.63	4.31
C_{oil}(eq), wt%	1.09	1.26	1.34	1.433
C_{wall}(eq), wt%	0.96	0.17	1.28	1.428
C_{oil}(eq) - C_{wall}(eq), wt%	0.14	0.09	0.06	0.005
$J_{wax,c} \times 10^{10}$, m/s·wt%	13.58	10.73	8.61	0.76

Table A.2 Comparison of the parameters for the characteristic mass flux for wax deposition, $J_{wax,c}$, among the deposition experiments when $\delta = 1$ mm with different $T_{coolant}$ temperatures, while Q_{oil} and T_{oil} are maintained constant.

Parameters	Value		
Experimental Operating Conditions			
T_{oil}, ^{0}C	20.2		
$T_{coolant}$, ^{0}C	5.0	10.0	15.0
Q_{oil}, m^3/h	5.0		
Model Calculations			
t, h	11.57	18.62	32.88
T_{wall}, ^{0}C	16.30	17.61	18.91
$D_{wo, wall} \times 10^{10}$, m^2/s	3.01	3.18	3.35
C_{oil} (eq), wt%	1.26	1.26	1.26
C_{wall} (eq), wt%	1.14	1.19	1.23
C_{oil} (eq) - C_{wall} (eq), wt%	0.12	0.07	0.03
$J_{wax,c} \times 10^{10}$, m/s·wt%	14.02	8.68	4.02

It can be seen that the conclusion that $J_{\text{wax,c}}$ increases with increasing T_{oil} and with increasing T_{coolant} is valid for $\delta > 0$.

Appendix B

Prediction of the Trend of Mass Driving Force at

Different Operation Temperatures

This appendix focused on establishing criterions as to whether the mass driving force increases or decreases as the oil/coolant temperature is changed. Since the concentration terms in mass driving force are calculated from solubility curve, it is necessary to first obtain the mathematical equation of solubility curve. Under most circumstances, the experimentally measured oil solubility curve can be fitted with a three-order polynomial equation, as shown in Equation (B.1)

$$C = aT^3 + bT^2 + cT + d \qquad \text{(B.1)}$$

Where T is temperature [℃], C is the equilibrium concentration of wax in oil [wt%], and a, b, c, and d are coefficients.

In the current discussion, the oil temperature, T_{oil} is changing while the coolant temperature, T_{cool} is holding as a constant. The opposite situation can be addressed using similar approach. Suppose when oil temperature changes from $T_{oil,1}$ to $T_{oil,2}$, wall temperature varies from $T_{wall,1}$ to $T_{wall,2}$, respectively. As a result, the change of C_{oil} and C_{wall} could be calculated in the way as shown in Equation (B.2) and (B.3).

$$\Delta C_{oil} = C_{oil,2} - C_{oil,1} = a(T_{oil,2}^3 - T_{oil,1}^3) + b(T_{oil,2}^2 - T_{oil,1}^2) + c(T_{oil,2} - T_{oil,1}) \qquad \text{(B.2)}$$

$$\Delta C_{\text{wall}} = C_{\text{wall},2} - C_{\text{wall},1} = a(T_{\text{wall},2}{}^3 - T_{\text{wall},1}{}^3) + b(T_{\text{wall},2}{}^2 - T_{\text{wall},1}{}^2) + c(T_{\text{wall},2} - T_{\text{wall},1}) \quad \text{(B.3)}$$

The mass driving force, $\Delta C = C_{\text{oil}} - C_{\text{wall}}$, will <u>increase</u> when $\Delta C_{oil} > \Delta C_{wall}$, namely

$$
\begin{aligned}
&a(T_{\text{oil},2}{}^3 - T_{\text{oil},1}{}^3 - T_{\text{wall},2}{}^3 + T_{\text{wall},1}{}^3) + b(T_{\text{oil},2}{}^2 - T_{\text{oil},1}{}^2 - T_{\text{wall},2}{}^2 + T_{\text{wall},1}{}^2) \\
&+ c(T_{\text{oil},2} - T_{\text{oil},1} - T_{\text{wall},2} + T_{\text{wall},1}) > 0
\end{aligned}
\quad \text{(B.4)}
$$

The mass driving force, $\Delta C = C_{\text{oil}} - C_{\text{wall}}$, will <u>decrease</u> when $\Delta C_{oil} < \Delta C_{wall}$, namely

$$
\begin{aligned}
&a(T_{\text{oil},2}{}^3 - T_{\text{oil},1}{}^3 - T_{\text{wall},2}{}^3 + T_{\text{wall},1}{}^3) + b(T_{\text{oil},2}{}^2 - T_{\text{oil},1}{}^2 - T_{\text{wall},2}{}^2 + T_{\text{wall},1}{}^2) \\
&+ c(T_{\text{oil},2} - T_{\text{oil},1} - T_{\text{wall},2} + T_{\text{wall},1}) < 0
\end{aligned}
\quad \text{(B.5)}
$$

BIBLIOGRAPHY

[1] EIA. Annual Energy Outlook. **2014**.

[2] Aiyejina A.; Chakrabarti, D. P.; Pilgrim A.; Sastry, M. K. S. Wax formation in oil pipelines: A critical review. *International Journal of Multiphase Flow*. **2011**, 37, 671-694.

[3] Hoepfner, M. E. Investigations into asphaltene deposition, stability, and structure. *Ph.D. Dissertation, University of Michigan*. **2013.**

[4] Creek, J. L.; Lund, H. J.; Brill, J. P.; Volk, M. Wax deposition in single phase flow. *Fluid Phase Equilibria.* **1999**, *158*, 801-811.

[5] Rønningsen, H. P. Production of waxy oils on the norwegian continental shelf: experiences, challenges, and practices. *Energy & Fuels*. **2012**, *26*, 4124-4136.

[6] Ragauskas, A. J.; Williams, C. K.; Davison, B. H.; Britovsek, G.; Cairney, J.; Eckert, C. A.; Frederick, W. J.; Hallett, J. P.; Leak, D. J.; Liotta, C. L.; Mielenz, J. R.; Murphy, R.; Templer, R.; Tschaplinski, T. The path forward for biofuels and biomaterials. *Science*. **2006**, *311*, 484-489.

[7] Levine, R. B. The production of algal biodiesel using hydrothermal carbonization and in situ transesterification. *Ph.D. Dissertation, University of Michigan*. **2013**

[8] Lee, H. S. Computational and rheological study of wax deposition and gelation in subsea pipelines. *Ph.D. Dissertation, University of Michigan*. **2007.**

[9] Armenta, R. E.; Valentine, M. C. Single-cell oils as a source of omega-3 fatty acids: an overview of recent advances. *Journal of the American Oil Chemists' Society*. **2012**, *90*, 167-182.

[10] Groom, M. J.; Gray, E. M.; Townsend, P. A. Biofuels and biodiversity: principles for creating better policies for biofuel production. *Conservation Biology*. **2008**, *22*, 602-609.

[11] Aguirre, A. -M.; Bassi, A.; Saxena, P. Engineering challenges in biodiesel production from microalgae. *Critical reviews in biotechnology*. **2013**, *33*, 293-308.

[12] Huang, Z.; Lee, H. S.; Senra, M, Fogler, H. S. A fundamental model of wax deposition in subsea oil pipelines. *AIChE J*. **2011**, *57*, 2955-2964.

[13] Gluyas, J. G.; Hichens, H. M. United kingdom oil and gas fields. Commemorative Millennium Volume. *Geological Society of London* **2003**, *20*, 327-333.

[14] Nguyen, D. A.; De Moraes, F. F.; Fogler, H. S. Fused Chemical Reactions. 3. Controlled release of a catalyst to control the temperature profile in tubular reactors. *Industrial & Engineering Chemistry Research* **2004**, *43*, 5862-5873.

[15] Niesen, V. G. The real cost of subsea pigging. *E&P Magazine* **2002** Available online: http://www.epmag.com/archives/features/3332.htm.

[16] Alyeska Pipeline Service Company. Low flow study-final report, June **2011**.

[17] Singh, P.; Venkatesan, R.; Fogler, H. S. Formation and aging of incipient thin film wax-oil gels. *AIChE J.* **2000**, *46*, 1059-1074.

[18] Jennings, D. W.; Weispfennig, K. Effects of shear and temperature on wax deposition: coldfinger investigation with a gulf of mexico crude oil. *Energy & Fuels* **2005**, *19*, 1376-1386.

[19] Paso, K; Fogler, H. S. Bulk stabilization in wax deposition systems. *Energy & Fuels* **2004**, *18*, 1005-1013.

[20] Bidmus, H. O.; Mehrotra, A. K. Solids deposition during "cold flow" of wax-solvent mixtures in a flow-loop apparatus with heat transfer. *Energy & Fuels* **2009**, *23*, 3184-3194.

[21] Hoffmann, R.; Amundsen, L. Single-phase wax deposition experiments. *Energy & Fuels* **2010**, *24*, 1069-1080.

[22] Han, S.; Huang, Z.; Senra, M.; Hoffmann, R.; Fogler, H. S. Method to determine the wax solubility curve in crude oil from centrifugation and high temperature gas chromatography measurements. *Energy & Fuels* **2010**, *24*, 1753-1761.

[23] Monrad, C. C.; Pelton, J. G. Heat transfer by convection in annular spaces. *Trans. AIChE* **1942**, *38*, 593-611.

[24] Van Driest, E. R. On turbulent flow near wall. *Journal of the Aeronautical Sciences***1956**, *23*, 1007-1011.

[25] Hayduk, W.; Minhas, B. S. Correlations for prediction of molecular diffusivities in liquids. *The Canadian Journal of Chemical Engineering* **1982**, *60*, 295-299.

[26] Bern, P. A.; Withers, V. R.; Cairns. J. R. Wax deposition in crude oil pipelines. In: *Proceedings of European Offshore Petroleum Conference and Exhibition* October 21-24 London, **1980**, 571-578.

[27] Burger, E. D.; Perkins, T. K.; Striegler, J. H. Studies of wax deposition in the trans-alaska pipeline. *Journal of Petroleum Technology* **1981**, 33, 1075-1086.

[28] Majeed, A.; Bringedal, B.; Overa, S. Model calculates wax deposition for n. sea oils. *Oil & Gas Journal* **1990**, 88, 63-69.

[29] Hamouda, A. A.; Davidsen, S. An approach for simulation of paraffin deposition in pipelines as a function of flow characteristics with a reference to teesside oil pipeline. In: *Proceedings of International Symposium on Oilfield Chemistry* Houston, **1995**, 459-470.

[30] Brown, T. S.; Niesen, V.G.; Erickson, D. D. Measurement and prediction of the kinetics of paraffin deposition. In: *Proceedings of SPE Technical Conference and Exhibition* Houston, **1993**, 353-368.

[31] Ribeiro, F.S.; Souza, M.; Paulo, R.; Braga, S. L. Obstruction of pipelines due to paraffin deposition during the flow of crude oils. *International Journal of Heat and Mass Transfer* **1997**, 40, 4319-4328.

[32] Asperger, A.; Engewald, W.; Fabian, G. Analytical characterization of natural waxes employing pyrolysis-gas chromatography-mass spectrometry. *Journal of Analytical and Applied Pyrolysis* **1999**, 52, 103-115.

[33] Venkatesan, R. The deposition and rheology of organic gels. *Ph.D. Dissertation, University of Michigan.* **2004**.

[34] Tinsley, J. F.; Prud'homme, R. K. Deposition apparatus to study the effects of polymers and asphaltenes upon wax deposition. *Journal of Petroleum Science and Engineering.* **2010**, 72, 166-174.

[35] Bidmus, H. O.; Mehrotra, A. K. Heat-transfer analogy for wax deposition from paraffinic mixtures. *Industrial & Engineering Chemistry Research.* **2004**, 43, 791-803.

[36] Parthasarathi, P.; Mehrotra, A. K. Solids deposition from multicomponent wax-solvent mixtures in a benchscale flow-loop apparatus with heat transfer. *Energy & Fuels* **2005,** *19,* 1387-1398

[37] Nelson, F.; Mehrotra, A. K. Deposition under turbulent flow of wax-solvent mixtures in a bench-scale flow-loop apparatus with heat transfer. *Energy & Fuels.* **2007**, 21, 1263-1276.

[38] Tiwary, R.; Mehrotra, A. K. Deposition from wax-solvent mixtures under turbulent flow: effects of shear rate and time on deposit properties. *Energy & Fuels*. **2009**, 23, 1299-1310.

[39] Matzain, A.; Apte, M. S.; Zhang, H. Q.; Volk, M.; Brill, J. P.; Creek, J. L. Investigation of paraffin deposition during multiphase flow in pipelines and wellbores-part 1: experiments. *Journal of Energy Resources Technology ASME*. **2002**, 124, 180-186.

[40] Singh, P.; Fogler, H. S.; Nagarajan, N. Prediction of the wax content of the incipient wax-oil gel in a flowloop: an application of the controlled-stress rheometer, *Journal of Rheology* **1999,** 43**,** 1437.

[41] Venkatesan, R.; Fogler, H.S. Comments on analogies for correlated heat and mass transfer in turbulent flow. *AIChE J*. **2004**, 50, 1623-1626.

[42] Monrad, C. C.; Pelton, J. G. Heat transfer by convection in annular spaces. *Trans. AIChE J*. **1942**, 38, 593-611.

[43] Deen, W. M. "Analysis of Transport Phenomena", Oxford, **1998**.

[44] Leite, G. B.; Abdelaziz, A. E. M.; Hallenbeck, P. C. Algal biofuels: Challenges and opportunities. *Bioresource Technology* **2013**, *145*, 134-141.

[45] Savage, P. E.; Hestekin, J. A. A perspective on algae, the environment, and energy. *Environmental Progress & Sustainable Energy* **2013**, *32*, 877-883.

[46] Lam, M. K.; Lee, K. T. Microalgae biofuels: A critical review of issues, problems and the way forward. *Biotechnology Advances* **2012**, *30*, 673-690.

[47] Greenwell, H. C.; Laurens, L. M. L.; Shields, R. J.; Lovitt, R. W.; Flynn, K. J. Placing microalgae on the biofuels priority list: A review of the technological challenges. *Journal of The Royal Society Interface* **2010**, *7*, 703-726.

[48] Wang, G.; Wang, T. Characterization of lipid components in two microalgae for biofuel application. *Journal of the American Oil Chemists' Society* **2011**, *89*, 135-143.

[49] Halim, R.; Danquah, M. K.; Webley, P. A. Extraction of oil from microalgae for biodiesel production: A review. *Biotechnology Advances* **2012**, *30*, 709-732.

[50] Grima, E. M.; Medina, A. R.; Giménez, A. G.; Pérez, J. A. S.; Camacho, F. G.; Sánchez, J. L. G. Comparison between extraction of lipids and fatty acids from microalgal biomass. *Journal of the American Oil Chemists' Society* **1994**, *71*, 955-959.

[51] Choi, S. A.; Oh, Y. K.; Jeong, M. J.; Kim, S. W.; Lee, J. S.; Park, J. Y. Effects of ionic liquid mixtures on lipid extraction from *Chlorella vulgaris*. *Renewable Energy* **2014**, *65*, 169-174.

[52] Kim, Y. -H.; Choi, Y. -K.; Park, J.; Lee, S.; Yang, Y. -H.; Kim, H. J.; Park, T. -J.; Kim, Y. H.; Lee, S. H. Ionic liquid-mediated extraction of lipids from algal biomass. *Bioresource Technology* **2012**, *109*, 312-325.

[53] U.S. Food and Drug Administration. *Use of chloroform as aningredient in cosmetic products*, Code of Federal Regulations, No. 21 CFR 700.18, 2013.

[54] Halim, R.; Gladman, B.; Danquah, M. K.; Webley, P. A. Oil extraction from microalgae for biodiesel production. *Bioresource Technology* **2011**, *102*, 178-185.

[55] Crampon, C.; Mouahid, A.; Toudji, S. -A. A.; Lépine, O.; Badens, E. Influence of pretreatment on supercritical CO_2 extraction from *Nannochloropsis oculata*. *The Journal of Supercritical Fluids* **2013**, *79*, 337-344.

[56] Levine, R. B.; Pinnarat, T.; Savage, P. E. Biodiesel production from wet algal biomass through in situ lipid hydrolysis and supercritical transesterification. *Energy & Fuels* **2010**, *24*, 5235-5243.

[57] Heilmann, S. M.; Davis, H. T.; Jader, L. R.; Lefebvre, P. A.; Sadowsky, M. J.; Schendel, F. J.; von Keitz, M. G.; Valentas, K. J. Hydrothermal carbonization of microalgae. *Biomass & Bioenergy* **2010**, *34*, 875-882.

[58] Levine, R. B.; Sierra, C. O. S.; Hockstad, R.; Obeid, W.; Hatcher, P. G.; Savage, P. E. The use of hydrothermal carbonization to recycle nutrients in algal biofuel production. *Environmental Progress & Sustainable Energy* **2013**, *32*, 962-975.

[59] Garcia Alba, L.; Torri, C.; Samorì C.; van der Spek, J.; Fabbri, D.; Kersten, S. R. A.; Brilman, D. W. F. (Wim). Hydrothermal treatment (HTT) of microalgae: Evaluation of the process as conversion method in an algae biorefinery concept. *Energy & Fuels* **2012**, *26*, 642-657.

[60] Heilmann, S. M.; Jader, L. R.; Sadowsky, M. J.; Schendel, F. J.; von Keitz, M. G.; Valentas, K. J. Hydrothermal carbonization of distiller's grains. *Biomass & Bioenergy* **2011**, *35*, 2526-2533.

[61] Heilmann, S. M.; Jader, L. R.; Harned, L. A.; Sadowsky, M. J.; Schendel, F. J.; Lefebvre, P. A.; von Keitz, M. G.; Valentas, K. J. Hydrothermal carbonization of microalgae II. Fatty acid, hydrochar, and algal nutrient products. *Applied Energy* **2011**, *88*, 3286-3290.

[62] Reddy, H. K.; Muppaneni, T.; Sun, Y.; Li, Y.; Ponnusamy, S.; Patil, P. D.; Dailey, P.; Schaub, T.; Holguin, F. O.; Dungan, B.; Cooke, P.; Lammers, P.; Voorhies, W.; Lu, X.; Deng, S. Subcritical water extraction of lipids from wet algae for biodiesel production. *Fuel* **2014**, *133*, 73-81.

[63] Siriwardhana, N.; Kalupahana, N. S.; Moustaid-Moussa, N. Health benefits of n-3 polyunsaturated fatty acids: eicosapentaenoic acid and docosahexaenoic acid. *Advances in Food and Nutrition Research* **2012**, *65*, 211-222.

[64] Gropper, S. S.; Smith, J. L. *Advanced nutrition and human metabolism*, Sixth Edition; Wadsworth: Belmont, CA, 2012.

[65] U.S. Food and Drug Administration. *Guidance for Industry, Q3C Impurities: Residual Solvents*, **1997**.

[66] Ackman, R. G.; Sipos, J. C. Application of specific response factors in the gas chromatographic analysis of methyl esters of fatty acids with flame ionization detectors. *Journal of the American Oil Chemists' Society* **1964**, *41*, 377-378.

[67] Vroom, K. E. The H-factor: A means of expressing cooking times and temperatures as a single variable. *Central Pulp & Paper Research Institute* **1957**, *38*, 228-231.

[68] Faeth, J. L.; Valdez, P. J.; Savage, P. E. Fast hydrothermal liquefaction of Nannochloropsis sp. to produce biocrude. *Energy & Fuels* **2013**, *27*, 1391-1398.

[69] Lu, Y.; Levine, R. B.; Savage, P. E. Fatty acids for nutraceuticals and biofuels from hydrothermal carbonization of microalgae. *Industrial & Engineering Chemistry Research* (In press). *http://dx.doi.org/10.1021/ie503448u*

[70] Resende, F. L. P.; Savage, P. E. Expanded and updated results for supercritical water gasification of cellulose and lignin in metal-free reactors. *Energy & Fuels* **2009**, *23*, 6213-6221.

[71] Guan, Q.; Savage, P. E.; Wei, C. Gasification of alga *Nannochloropsis sp.* in supercritical water. *The Journal of Supercritical Fluids* **2012**, *61*, 139-145.

[72] Cherad, R.; Onwudili, J. A.; Ekpo, U.; Williams, P. T.; Lea-langton, A. R.; Carmargo-Valero, M.; Ross, A. B. Macroalgae supercritical water gasification combined with nutrient recycling for microalgae cultivation. *Environmental Progress & Sustainable Energy* **2013**, *32*, 902-909.

[73] Karayildirim, T.; Sinag, A.; Kruse, A. Char and coke formation as unwanted side reaction of the hydrothermal biomass gasification. *Chemical Engineering and Technology* **2008**, *1*, 1561-1573.

[74] Castello, D.; Kruse, A.; Fiori, L. Supercritical water gasification of hydrochar. *Chemical Engineering Research and Design* **2014**, *92*, 1864-1875.

[75] Resende, F. L. P.; Savage, P. E. Kinetic model for noncatalytic supercritical water gasification of cellulose and lignin. *AICHE J.* **2010**, *56*, 2412-2420.

[76] Guan, Q.; Wei, C.; Savage, P. E. Kinetic model for supercritical water gasification of algae. *Physical Chemistry Chemical Physics* **2012**, *14*, 3140-3147.

[77] Brown, T. M.; Duan, P. G.; Savage, P. E. Hydrothermal liquefaction and gasification of *Nannochloropsis sp. Energy & Fuels* **2010**, *24*, 3639-3646.

[78] Chakinala, A. G.; Brilman, D. W. F. W.; Swaaij, W. P. M. van; Kersten, S. R. A. Catalytic and non-catalytic supercritical water gasification of microalgae and glycerol. *Industrial & Engineering Chemistry Research* **2010**, *49*, 1113-1122.

[79] Guan, Q., Wei, C.; Savage, P. E. Hydrothermal gasification of Nannochloropsis sp. with Ru/C. Energy & Fuels 2012, 26, 4575-4582.

[80] Lardon, L.; Helias, A.; Sialve, B.; Steyer, J. -P.; Bernard, O. Life-cycle assessment of biodiesel production from microalgae. *Environmental Science & Technology* **2009**, *43*, 6475-6481.